Computational model of chimeric antigen receptors explains site-specific phosphorylation kinetics

Jennifer A. Rohrs[1], Dongqing Zheng[2], Nicholas A. Graham[2], Pin Wang[1,2], Stacey D. Finley[1,2,*]

[1]Department of Biomedical Engineering, University of Southern California, Los Angeles, CA, USA, 90089
[2]Mork Family Department of Chemical Engineering and Materials Science, University of Southern California, Los Angeles, CA, USA, 90089

Running title: Model of CAR phosphorylation kinetics

***Corresponding Author:**
Stacey D. Finley
1042 Downey Way, DRB 140
Los Angeles, CA 90089
Phone: 213-740-8788; Fax: 213-821-3897
Email: sfinley@usc.edu

Abstract
Chimeric antigen receptors (CARs) have recently been approved for the treatment of hematological malignancies, but our lack of understanding of the basic mechanisms that activate these proteins has made it difficult to optimize and control CAR-based therapies. In this study, we use phospho-proteomic mass spectrometry and mechanistic computational modeling to quantify the *in vitro* kinetics of individual tyrosine phosphorylation on a variety of CARs. We show that the ten tyrosine sites on the CD28-CD3ζ CAR are phosphorylated by LCK independently and with different kinetics. The addition of CD28 at the N-terminal of CD3ζ increases the overall rate of CD3ζ phosphorylation. Our computational model explains experimental observations of CD3ζ immunoreceptor tyrosine-based activation motif (ITAM) phosphorylation and provides new mechanistic hypotheses for how these activating domains can be more optimally phosphorylated. Specifically, the model highlights the importance of protein binding to single ITAM tyrosine sites to enhance the amount of doubly phosphorylated ITAMs. This quantitative modeling framework can be used to better understand CAR signaling and T cell activation.

Introduction
One of most widely used methods for engineering a patient's T cells to fight cancer is through the expression of chimeric antigen receptors (CARs). CARs are proteins that combine an extracellular antibody-derived targeting domain with intracellular T cell activating domains derived from the endogenous T cell receptor (Fesnak *et al*, 2016). These engineered T cells have emerged as promising treatments for hematopoietic cancers (Firor *et al*, 2015; Mullard, 2017)**;** however, not all patients respond to treatment and it has been difficult to expand these therapies to solid tumors (Kingwell, 2017; Morgan *et al*, 2010; Lee *et al*, 2015; Moon *et al*, 2014). Significantly, it has recently been shown that CARs are less effective in activating T cells than engineered T cell receptors (TCRs) (Harris *et al*, 2018). More work needs to be done to better understand the mechanisms through which CAR-engineered T cells become activated so that they can be more optimally designed and expanded to a wider patient population. In this study, we use quantitative phospho-proteomic mass spectrometry and computational modeling to explore the mechanisms that lead to the phosphorylation of CAR proteins. Computational models, like the one developed here, provide a unique method to use basic engineering principles to better understand and optimize the signaling pathways that activate CAR-engineered T cells.

The CAR-T cell therapy Yescarta was approved by the FDA in October 2017 and contains signaling domains derived from the CD3ζ domain of the T cell receptor (TCR) and the CD28 co-stimulatory domain (Mullard, 2017). These T cell signaling domains are phosphorylated by the Src family kinases, the most important of which in endogenous T cells is lymphocyte-specific protein tyrosine kinase (LCK) (Palacios & Weiss, 2004; Lovatt *et al*, 2006; Nika *et al*, 2010). CD3ζ contains six tyrosine phosphorylation sites, arranged in pairs on three immunoreceptor tyrosine-based activation motifs (ITAMs) (**Figure 1A**) (Chakraborty & Weiss, 2014). When doubly phosphorylated, these ITAMs can bind to the adaptor protein ZAP-70, allowing LCK to phosphorylate ZAP-70 and also protecting the CD3ζ ITAMs from dephosphorylation (Au-Yeung *et al*, 2009; Sjölin-goodfellow *et al*, 2015). Interestingly, in unstimulated lymphocytes and peripheral T cells, CD3ζ is constitutively phosphorylated at the two C-terminal ITAMs (ITAMs B and C), resulting in a 21 kDa protein (van Oers *et al*, 2000; Pitcher *et al*, 2003). Upon full activation, all three ITAMs become phosphorylated to produce the 23 kDa form. Although the key phosphorylation sites are readily known, the order and kinetics of their

phosphorylation have not been quantitatively studied. Thus, the mechanism through which the 21- and 23 kDa phosphorylated species form is not known, making it difficult to control the activation of CARs.

Combining the CD3ζ activating domain and a co-stimulatory domain on the same protein adds additional complexity to the CAR. The CD28 co-stimulatory domain has four tyrosine sites, which can be phosphorylated by LCK (Boomer & Green, 2010), and may also influence the catalytic activity of LCK (Holdorf *et al*, 2002; Carey *et al*, 2000). Once phosphorylated, CD28 tyrosine sites bind to various adaptor proteins that are also phosphorylated downstream of CD3ζ (Tian *et al*, 2015). Thus, CD28 can tune the response to CD3ζ activation. Additionally, the recruitment and competition by CD28 for LCK may alter the phosphorylation of CD3ζ.

All ten of the tyrsoine sites on CD3ζ and CD28 work together, in different ways, to affect the downstream signaling that controls T cell activation responses such as cytotoxicity, cytokine production, proliferation, and survival (Teng *et al*, 1996; Lu *et al*, 1994; Michel *et al*, 2001; Chae *et al*, 2004; Kersh *et al*, 1999). By better understanding how these chimeric proteins are phosphorylated, we can identify ways to tune them to create more optimal CAR therapies. In this study, we have explored the kinetics of CD3ζ and CD28 phosphorylation in detail. We paired a recombinant protein system with phospho-proteomic mass spectrometry to measure the site-specific phosphorylation of CAR proteins by LCK over time. To our knowledge, this is the first study to quantify phosphorylation at individual sites on the intact CAR protein. We then fit this data using a computational model to robustly quantify the differences between the phosphorylation kinetics of the ten tyrosine sites. We used the computational model to generate new predictions regarding the mechanisms that allow for the emergence of the 21 kDa partially phosphorylated form of CD3ζ. We can use the novel insights from this study to continue expanding our understanding of CAR-mediated T cell activation and better engineer future CAR therapies.

Results

The six tyrosine sites on CD3ζ are phosphorylated by LCK with different kinetics

We first sought to explore how LCK phosphorylates the six tyrosine sites on CD3ζ. To do this, we utilized a liposome-based recombinant protein system, developed by Hui and Vale (Hui & Vale, 2014). In this system, his-tagged proteins are bound to nickel chelating lipids on the surface of large unilamellar liposomes, as shown in **Figure 1A**. Since the CAR and LCK proteins are largely membrane bound in T cells, this system allows us to mimic the two-dimensional protein arrangement and more accurately capture the true kinetics of the interactions between these proteins.

The liposome-bound proteins were allowed to react in the presence of ATP, and we performed phospho-proteomic mass spectrometry to specifically measure the phosphorylation at each ITAM site over time. To quantify the site-specific phosphorylation, we needed to directly compare the mass spectrometry intensity of phosphorylated and unphosphorylated peptide pairs. To do this, we used a standard curve with a known ratio of phosphorylated:unphosphorylated peptide (**Supplemental Figure S1**) (Lee *et al*, 2002). Additionally, we needed to ensure that there is only one tyrosine site on each tryptic peptide. This is true for all CD3ζ ITAM tyrosine sites except A1 (**Figure 1B**). The peptide containing site A1 also contains a tyrosine at position 64,

which is not part of an ITAM and has not been shown to play a significant role in T cell activation. Therefore, we added a Y64F mutation in the CD3ζ recombinant protein. In this way, we were able to normalize the phosphorylated:unphosphorylated intensity ratios for each ITAM site in our time courses by the standard curves, thus calculating the percent phosphorylation over time for each of tyrosine sites of interest.

Figure 1C (dots) shows the percent phosphorylation of each of the six ITAM sites over time on liposomes that contain 10% acidic phosphatidylserine (POPS) lipids, which is similar to the concentration of phosphatidylserine on the inner leaflet of the T cell plasma membrane (Hui & Vale, 2014). Our measurements show that not all of the sites are phosphorylated at the same rate. To quantify the differences, we fit these data to a four-parameter sigmoidal curve, estimating the half maximal time and the Hill coefficient for each site (**Supplemental Figure S2**). The half maximal times show that the six sites are phosphorylated with different kinetics (A1>B2>B1≥A2≥C2>C1). In comparison, the Hill coefficient for all tyrosine phosphorylation sites is close to one.

LCK catalyzes CD3ζ tyrosine site with different substrate specificities

To better understand the underlying mechanism of phosphorylation of the specific tyrosine sites on CD3ζ, we used mass action kinetics to construct a computational model of CD3ζ phosphorylation by LCK. Fitting a sigmoidal curve to the experimental data and determining the half maximal time and Hill coefficient are a standard means of characterizing the relative phosphorylation rates; however, we aim to provide a mechanistic examination CD3ζ phosphorylation kinetics. Therefore, we used a molecular-detailed kinetic model of LCK-CD3ζ interactions.

We tested two different model structures to see which best fit the CD3ζ site-specific phosphorylation data: a sequential order and a random order. In the sequential order model, LCK can phosphorylate the six sites at different rates, but in a specified order defined by the order of the half maximal time from the sigmoidal fit (**Supplemental Figure S2B**). This model leads to a consistent increase in the Hill coefficient as it progresses through the sequence of ITAM phosphorylation sites (A1, B2, B1, A2, C2, and C1) (**Supplemental Figure S3A-C**). On the other hand, in the random order model, each of the six ITAM sites interact with LCK independently. With this model structure, each of the sites have the same Hill coefficient, which is consistent with the experimental data (**Supplemental Figure S3D-F)**. Additionally, the random order model fits the data better, with a lower residual error, than the sequential model. Upon visual inspection, we can see that the random order model better captures the overall trends of the data, specifically for the graduate approach to saturation. Therefore, we proceeded with the model mechanism that uses a random order of phosphorylation to fit our data.

We fit the experimentally determined phosphorylation levels using this random order model structure in which all of the ITAMs interact with LCK independently (**Figure 1C, lines**), and estimated the site-specific kinetic phosphorylation parameters. For each tyrosine site time course and lipid formulation, 50 rounds of model parameter fitting gave nearly identical fits to the data. The substrate specificities (see methods), calculated from the model parameters fit to the data, were also consistent across the different parameter fits for a single biological replicate. **Figure 1D** shows the substrate specificity of LCK at each CD3ζ ITAM site.

The values of the estimated substrate specificities follow the same overall order as the half maximal times derived from the simple sigmoidal fit (**Supplemental Figure 2B**). However, the substrate specificity gives us additional information about the relative preference that LCK has for each of the sites. While the difference between the half maximal time of ITAM pairs (A1-A2, B1-B2, and C1-C2) are very similar, the same cannot be said for the substrate specificity. There is a much larger difference between the substrate specificity of sites A1 and A2 than there is between B1 and B2. This difference is even smaller between C1 and C2. That is, even though the two sites on ITAM C have a relatively large difference in their half maximal phosphorylation times, LCK's preference for these two sites is nearly identical. In comparison, for ITAM A, LCK has a much higher preference for site A1 than it does for site A2.

The CD3ζ ITAM sites are phosphorylated independently

We wanted to confirm the model prediction that the sites are phosphorylated independently by testing for interactions between the CD3ζ ITAM sites. Specifically, we wanted to identify if there are any binding or competitive effects that influence the kinetics at distant sites. Therefore, we individually mutated each tyrosine site to a phenylalanine and measured the percent phosphorylation over time of the other sites.

We also investigated the effect of the liposome membrane acidity. Several T cell receptor proteins, including the closely related CD3ε and CD28 proteins, have been shown to have basic residues in their intracellular domains that can interact with acidic lipids on the inner leaflet of the T cell membrane (Aivazian & Stern, 2000; Dobbins *et al*, 2016; Gagnon *et al*, 2012). These interactions are thought to help limit tyrosine accessibility, thus controlling aberrant phosphorylation in unstimulated cells. Therefore, we also tested if CD3ζ interactions with the acidic POPS lipids in the liposome membrane were contributing to the different rates of phosphorylation seen in the site-specific data.

Figure 2A shows the overlay of all of the phosphorylation time course experiments (six individual CD3ζ Y to F point mutations, wild type CD3ζ stimulated on 0% and 45% POPS liposomes, and two biological replicates of wild type CD3ζ stimulated on 10% POPS liposomes) for each site. The trends for all of the site-specific time courses are very similar, indicating that neither individual site mutations or changes to the acidic lipid microenvironment significantly affect the phosphorylation kinetics of CD3ζ tyrosine sites. To compare between the sites, we grouped the time course responses together for all of the experimental conditions and used the pair-wise Tukey t-test to identify which ITAM site phosphorylation levels were significantly different from the others (**Figure 2B**). We compared the data sets at two different time points 10 minutes (blue), which is close to the half maximal time of the quickly phosphorylated ITAM sites A1 and B2, and 60 minutes (orange), which is close to the half maximal time of the majority of the other sites. The 10-minute comparison shows that A2, C1, and C2 are not significantly different from each other, while site B1 is significantly different from A2 and C1 but not C2. From both the 10-minute and 60-minute comparisons, we see that sites A1 and B2 are both significantly different from all other sites.

We next fit our mechanistic kinetic model to each of these data sets. Each experimental time course was fit to the data independently 50 times (**Supplemental Figure S4**). We again found that the model consistently fit the data well, giving nearly identical calculations of substrate specificity for each data set. **Figure 2C** shows the mean and

standard deviation of the LCK substrate specificity between all of the experimental conditions. Although only site A1 is significantly different from all other sites, the trends between the sites for a given experiment are highly consistent. This analysis confirms that the CD3ζ ITAM tyrosine sites are phosphorylated independently and without a dependence on the acidic lipid microenvironment, as mutating individual sites or lipid concentrations does not significantly affect the site-specific phosphorylation dynamics of CD3ζ.

LCK binding and catalytic parameters are correlated

The molecular-detailed nature of the model allows us to investigate how particular molecular interactions and catalytic events influence CD3ζ phosphorylation. In model fitting, we noticed that while the individual parameters could vary widely, the predicted phosphorylation levels and estimated substrate specificities given by the model fits were nearly identical. To further explore how LCK binding and catalytic activities relate, we held the association rate constant, which has been shown to be better constrained than the dissociation rate (Schlosshauer & Baker, 2004), and allowed the dissociation and catalytic rates to vary. **Figure 3A** shows how the resulting half maximal time of the phosphorylation curve shifts with different parameter combinations. In general, we found that the dissociation and catalytic rate parameters are directly correlated, with approximately linear contour lines on the resulting heat maps. However, as the dissociation rate decreases, the contour lines begin to plateau. In this region of low dissociation and catalytic rates, the majority of the LCK remains bound to the site without dissociating or phosphorylating (**Figure 3B**). For all ITAM sites, greatly reducing the dissociation rate can lead to this sink-like effect for LCK. In general, the dissociation rate and catalytic rate are directly related, and changing them together will change the binding of LCK without influencing CD3ζ phosphorylation, or the model fit to the data.

Computational model predicts the emergence of 21 kDa CD3ζ in the presence of ZAP-70 and phosphatases

We next wanted to better understand how the 21 kDa form of CD3ζ could be preferentially phosphorylated on ITAMs B and C, despite the fact that these sites are phosphorylated more slowly than those on ITAM A. ZAP-70 is able to bind to doubly phosphorylated ITAMs and protect them from dephosphorylation, and these two mechanisms together are sufficient for the production the 21 kDa form of CD3ζ when reconstituted in COS 7 cells (van Oers *et al*, 2000). Therefore, we extended our computational model to explore the occurrence of the 21 and 23 kDa forms of CD3ζ in the presence of ZAP-70 binding and phosphatase activity. To specifically explore the effects of these new parameters, we first refit the data set from **Figure 1C** using the parameter constrains described above in which the association rate is the same for all sites. Although multiple sets of parameters (along a particular contour line in **Figure 3A**) gave similar fits to the data, we chose one set to begin our analysis (**Dots in Figure 3**, **parameters listed in supplemental Table S1**).

We tested a range of ZAP-70 binding and phosphatase parameters using initial conditions with a 1:1:1 ratio of LCK:CD3ζ:ZAP-70, and recorded the steady state phosphorylation levels of each ITAM (**Figure 4A**). All of the ITAMs were either unphosphorylated or doubly phosphorylated, with negligible amounts of singly phosphorylated ITAMs. These graphs show that there is a range of phosphatase activity and ZAP-70 binding parameters that will allow for ITAM B and C to be phosphorylated at

similar levels and for ITAM A to be significantly less phosphorylated (**Figure 4A red dashed region**), indicating that this is a robust response of the system. The time course response of ITAM phosphorylation in the presence of phosphatase activity and ZAP-70 binding is shown in **Figure 4B**. Solid lines represent the time course for the phosphatase and ZAP-70 parameters at the point of the red dot in **Figure 4A**. The shaded regions are the 95% confidence interval for the range of parameters shown within the red dashed areas on **Figure 4A**. For all parameters within the red dashed area, at steady state, ITAMs B and C are significantly more phosphorylated than ITAM A. In general, the parameter range in the red dashed area is characterized by high phosphatase activity and strong ZAP-70 binding. Given the observations that phosphatases, like CD45, are highly expressed and in close proximity to the TCR and/or CARs in resting T cells, the model captures how this high phosphatase activity can result in the 21 kDa form of CD3ζ cells (Bu *et al*, 1995; Stanford *et al*, 2012).

It is also known that when the immunological synapse forms upon both TCR and CAR T cell activation, phosphatases with large extracellular regions are excluded, reducing the local phosphatase activity (Leupin *et al*, 2000); however, in **Figure 4A**, low levels of phosphatase activity result in activation of only ITAM A and B, but not ITAM C, meaning that this cannot recreate the 23 kDa form of fully phosphorylated CD3ζ. Therefore, we continued to explore the model to better understand how CD3ζ could become fully phosphorylated. It has also been shown that upon initiation of the immunological synapse, downstream signaling molecules, like ZAP-70, are recruited to the area (Jenkins *et al*, 2014; Ilani *et al*, 2007). We therefore wanted to see how increasing the amount of ZAP-70 would affect CD3ζ phosphorylation in the model. **Figure 4C** shows the steady state levels of doubly phosphorylated ITAMs for an initial condition ratio of 1:1:3 for LCK:CD3ζ:ZAP-70. In the black dashed region of **Figure 4C,** we see that reducing the phosphatase activity in the presence of this higher level of ZAP-70 can lead to the emergence of the fully phosphorylated form of CD3ζ. The time course of activation is shown in **Figure 4D.** Importantly, even with the high ZAP-70 concentration, increasing the phosphatase activity will still result in a 21 kDa form of CD3ζ in which ITAMs B and C are more phosphorylated than ITAM A (**Figure 4C**, red dashed region). The model can mimic the environment of resting and activated T cells, allowing us to identify the parameter region that can govern the emergence of two biologically relevant forms of phosphorylated CD3ζ.

LCK binding helps protect slowly phosphorylated ITAMs from dephosphorylation

To explore the mechanism through which more slowly phosphorylated ITAMs reach higher steady state levels of phosphorylation than the quickly phosphorylated ITAMs in the 21 kDa form of CD3ζ, we investigated how LCK binding influences the system. To do this, we altered the catalytic and dissociation rates of LCK together for each ITAM site along the contour lines shown in **Figure 3**. As the substrate specificity depends on only the parameter values (see methods), maintaining the same fold change between the dissociation and catalytic rates will keep the same substrate specificity. In this way, the binding activity of LCK changes, but the fit to our experimental data remains the same. The ZAP-70 binding and phosphatase activity parameters were held constant at the values indicated by the red dot in **Figure 4A**, in the region that allows for the emergence of this 21 kDa form.

We applied this model to predict how varying the dissociation and catalytic rates at one ITAM affects phosphorylation of other ITAMs on CD3ζ. We allowed the dissociation

rates to vary within the linear region of **Figure 3** (10^3-10^9 min^{-1}), and we matched the catalytic rates to agree with the average site-specific substrate specificities across all experiments (shown in **Figure 2C**). **Figure 5A** shows how changing the LCK binding kinetics of ITAM A tyrosine sites affects the steady state phosphorylation percent of each ITAM. The dissociation rates for ITAM A1 and A2 are shown on the x- and y- axes, respectively. Changing the catalytic and dissociation rates of these sites influences the overall phosphorylation of the system. When the rates of are reduced, LCK is slower to dissociate from or phosphorylate the sites on ITAM A, resulting in more LCK bound to the site (**Figure 5B**).

Since the phosphatases can only act on ITAMs without bound LCK, this results in more protection of partially phosphorylated ITAM A, allowing the necessary time for LCK to create doubly phosphorylated ITAM A. As more LCK binds to ITAM site A2, less of it is available to bind and protect ITAMS B and C. Therefore, as the binding of LCK to ITAM A increases, the steady state phosphorylation of ITAMs B and C are reduced. Similar effects can be seen for changes to the LCK kinetics on ITAM B (**Figure 5C, D**) and ITAM C (**Figure 5E, F**). This analysis shows that LCK binding and protection of partially phosphorylated ITAMs is the dominant mechanism in the model that allows for ITAM sites that are phosphorylated at a slower rate to become more phosphorylated at steady state. Altogether, the model predictions presented thus far enable a better understanding of how LCK binds to and phosphorylates the CD3ζ intracellular domain.

CD28 tyrosine sites are phosphorylated more slowly than CD3ζ tyrosine sites

Next, we investigated how the addition of a co-stimulatory domain, like CD28, could influence CAR phosphorylation. To test this, we inserted the intracellular domain of CD28 at the N-terminal of CD3ζ (28ζ), the same configuration typically used in the CAR constructs evaluated in pre-clinical studies and clinical trials (**Figure 6A**). CD28 has four tyrosine sites, each of which can be phosphorylated by LCK. We again used phospho-proteomic mass spectrometry to quantify the site-specific phosphorylation levels of 28ζ. **Figure 6B** shows the sequence and trypsin cut sites of the CD28 intracellular domain, in which the second and third tyrosine sites in CD28 (Y206 and Y209) are both on the same peptide after trypsin digestion. Therefore, to individually measure the phosphorylation rates of these two sites, we made two more proteins with a tyrosine to phenylalanine mutation at each of these sites (28ζ-Y206F, and 28ζ-Y209F).

Interestingly, our measurements indicate that Y209 phosphorylation is required for the phosphorylation of Y206. **Figure 6C** shows the individual CD28 tyrosine site phosphorylation time courses for each of the three CD28-CD3ζ recombinant proteins. From these graphs, we can see that there is no significant phosphorylation of the Y206 site without prior phosphorylation of Y209 (teal lines).

The estimated substrate specificities provide insight into the effects of particular CD28 tyrosine sites. We fit the phosphorylation measurements with a computational model that includes CD28 and estimated the substrate specificities for each site. The model fits the data well (**Figure 6C**, lines). In agreement with the literature (Hui *et al*, 2017), all tyrosine sites on CD28 are phosphorylated more slowly than the CD3ζ tyrosine sites. The model calculated substrate specificities for each of these sites are shown in **Figure 6D**. From the Y206F and Y209F mutants, we can see that mutating these sites reduces the overall phosphorylation rates of the CD28 protein, with the Y209F mutation displaying the

strongest effect. This indicates that Y209, and to a lesser extent Y206, play a significant role in either the recruitment or phosphorylation activity of LCK toward CD28.

CD28 increases the phosphorylation rate of CD3ζ

CD28 influences the overall phosphorylation rate of CD3ζ, as well as the individual phosphorylation rate of site C2. **Figure 7A** shows the phosphorylation time courses (dots) and model fits (lines) of CD3ζ ITAM sites on the three CD28-CD3ζ recombinant proteins. Wildtype CD28 increases the overall phosphorylation rate of all CD3ζ tyrosine sites, making it difficult to distinguish a specific order of phosphorylation in the 28ζ recombinant protein. Similar to the CD28 results shown in **Figure 6C**, this change in substrate specificity is largely dependent on the presence of CD28-Y209, and, to a lesser extent, CD28-Y206. This can also be seen in the estimated substrate specificity values (**Figure 7B**).

In addition to shifting the overall substrate specificity of the protein as a whole, CD28 also changes the relative order of the CD3ζ tyrosine site phosphorylation rates. Site C2, which had one of the lowest substrate specificities in the CD3ζ-only recombinant protein (**Figure 1F**), has one of the highest substrate specificities on the CD28-CD3ζ proteins (**Figure 7B**). This relative change in the phosphorylation rate order is not influenced by mutations at site Y206 or Y209, as the substrate specificity of this site relative to the other sites does not change with the CD28 mutants.

CD28 may decrease the threshold of CD3ζ ITAM activation

To explore how the CD28-driven changes to the relative order of CD3ζ tyrosine phosphorylation would influence the steady state phosphorylation of the ITAMs, we returned to our ZAP binding dephosphorylation model. Using the phosphatase and ZAP-70 binding parameters from the CD3ζ model, we varied the LCK binding and catalytic rates, as we did in **Figure 5**, to verify that the same mechanism of LCK binding was still important in this system (**Supplemental Figure S5**). We then chose a set of LCK parameters that would allow the 21 kDa form of CD3ζ to emerge while still fitting our 28ζ ITAM phosphorylation data (**parameters listed in in Supplemental Table S1**).

We next varied the phosphatase and ZAP-70 binding parameters, as we did in **Figure 4A**, using the 1:1:1 initial condition ratio for LCK:CD3ζ:ZAP-70. **Figure 7C** shows the resulting steady state phosphorylation levels of each ITAM on 28ζ. The red dashed region shows that the 21 kDa form of CD3ζ is produced in the same parameter region as it was in the CD3ζ-only model in **Figure 4A**, again highlighting the robustness of the model predictions. The time course of the phosphorylation level for this parameter region is shown in **Figure 7D**. Interestingly, however, with the increase to the phosphorylation rate of CD3ζ site C2, we now see that even with the low ZAP-70 ratio, about 30% of CD3ζ can become fully phosphorylated at low phosphatase activity. This percentage is limited only by the 3:1 ration of CD3ζ ITAM binding sites to ZAP-70 molecules. The time course for this region is shown in **Figure 7E**. These results indicate that the increase in phosphorylation rates of CD3ζ on the 28ζ protein may result in a lower activation threshold for the 28ζ CAR phosphorylation, as CD3ζ on this protein may be able to become fully phosphorylated in the presence of lower ZAP-70 concentrations or higher phosphatase activity.

Discussion

In this study, we used phospho-proteomic mass spectrometry and computational modeling to quantitatively assess the mechanism of CD3ζ and CD28 intracellular phosphorylation in a CAR construct. By measuring the phosphorylation of individual tyrosine sites on CD3ζ and CD28 over time, we showed that the six sites on CD3ζ and four sites on CD28 are phosphorylated at different rates. Individual CD3ζ point mutations showed that the site-specific kinetics are largely independent, and therefore removing one site will not greatly influence phosphorylation at any of the other sites. Additionally, attaching CD28 to the N-terminal of CD3ζ increased the overall phosphorylation rate of the protein, and particularly increased the relative rate of phosphorylation at the C2 ITAM site.

Interestingly, we did not see any effect of acidic lipid concentration on the phosphorylation rates of CD3ζ tyrosine sites. Previous studies have reported different effects of acidic lipids on CD3-family protein phosphorylation. Several studies have indicated that acidic lipids in the plasma membrane can control aberrant phosphorylation of CD3ε and CD28 in unstimulated cells through binding of basic residues in the protein to acidic lipids in the plasma membrane (Aivazian & Stern, 2000; Dobbins *et al*, 2016; Gagnon *et al*, 2012). In addition, Hui and Vale saw that ZAP-70 tandem SH2 domains were able to bind more quickly as CD3ζ became phosphorylated in a system containing 10% acidic POPS lipids compared to 0% POPS lipids (Hui & Vale, 2014). In our system, changing the concentration of acidic POPS lipids on the liposome surface (even up to 45% POPS) did not change the rate of phosphorylation of the protein as a whole or the relative phosphorylation rate order of the individual sites. Therefore, we believe that the acidic lipid concentration does not directly affect the phosphorylation of CD3ζ; but, as Hui and Vale showed, it may influence the binding kinetics of downstream proteins like ZAP-70 by more readily recruiting these proteins to membrane regions with acidic lipids.

We constructed a computational model to further investigate the mechanisms that lead to CD3ζ phosphorylation. With the model, we were able to calculate site-specific phosphorylation parameters, such as the LCK substrate specificity, that are difficult to measure experimentally. Previous studies have attempted to use CD3ζ phospho-tyrosine specific antibodies to qualitatively define the phosphorylation order of individual ITAM sites (Kersh, 1998); but, the similarity between ITAM sites limited the antibody specificity, preventing solid conclusions regarding the phosphorylation order. In 2003, Housden et al. used synthetic peptides that each contained one ITAM tyrosine to measure the preference of LCK for each site through radioactive phosphate incorporation. Interestingly, the LCK substrate specificity order they found (A1>C1>C2>B1>A2>B2) differs from ours (A1>B2>B1>A2≥C2≥C1) (Housden *et al*, 2003). Their experiments were performed in solution, not in a two-dimensional lipid-bound configuration, and each single tyrosine-bearing peptide was phosphorylated independently. Therefore, their study did not account for conformational, steric, and competitive factors that may influence the phosphorylation rates at different sites. However, the authors did use mass spectrometry to measure full length recombinant protein CD3ζ phosphorylation and found that, at intermediate time points, ITAM site A1 was significantly more phosphorylated than the other sites, which is consistent with our data. To our knowledge, our work is the first study to specifically quantify the individual phosphorylation kinetics of all six CD3ζ ITAM tyrosine sites on the same protein in a two-dimensional lipid-bound setting.

Our model provides novel insights into the effects of LCK-CD3ζ interactions. Our modeling results confirm a random order of LCK phosphorylation of CD3ζ, validating previous studies in the literature based on average CD3ζ protein phosphorylation (Mukhopadhyay *et al*, 2016). Additionally, we were able to provide a possible mechanistic explanation for how the slowly phosphorylated ITAMs B and C become more phosphorylated than ITAM A at steady state in the 21 kDa form of CD3ζ (van Oers *et al*, 2000; Pitcher *et al*, 2003). The model indicates that, while the rates of phosphorylation and dephosphorylation are important, the binding events that protect the ITAMs from dephosphorylation are also important. These effects of LCK binding predicted by our model have also been hypothesized in previously published models based on experimental data (Sjölin-goodfellow *et al*, 2015).

Importantly, LCK is not the only protein that could bind and protect these single ITAM sites. In future work, the model can be applied to include the binding of other proteins in the T cell activation pathway that can bind to single ITAM sites, allowing us to study a range of molecular interactions and their effects on CAR phosphorylation. These modeling results, as well as the site-specific quantification results, indicate that protein-protein binding interactions, the two-dimensional protein arrangement, and the arrangement of the tyrosine sites on CD3ζ may all play a role in determining the different substrate specificities of LCK toward each ITAM site.

CD28 also plays an important role in the CAR structure, both by adding its co-stimulatory signaling and modulating the phosphorylation rates of CD3ζ. We showed that adding CD28 to the N-terminal of CD3ζ increases the overall phosphorylation of CD3ζ, and this is largely dependent on CD28-Y209. This site has been implicated in the recruitment of LCK to the immunological synapse in endogenous T cells through binding of the SH2 domain on LCK (Hofinger & Sticht, 2005). Here, we validate the importance of this site as a strong recruiter of LCK, and its potential role in the strong activation of CD28-bearing CAR proteins.

Interestingly, CD28-Y209 is phosphorylated much more slowly than any of the sites on CD3ζ. In fact, when all of the CD3ζ sites are 100% phosphorylated, only about 25% of the CD28-Y209 sites have been phosphorylated. This leads us to hypothesize that unphosphorylated Y209 plays a role in recruiting LCK to the system. Perhaps this site is able to bind and recruit LCK more readily than other sites but, given its lower affinity for the catalytic pocket of LCK, it can be outcompeted by other sites on the same protein. More work needs to be done to decouple the binding preferences that lead to LCK recruitment from the catalytic activity of the protein-substrate pairs.

We used our computational model to explore the effects of the CD28-dependent increase and reordering of CD3ζ ITAM phosphorylation. The model predicts that increasing the phosphorylation rate of ITAM site C2 in the presence of CD28 could allow the maximal level of ITAM C phosphorylation to increase above that of the CD3ζ-only protein. This effect appears to be independent of phosphorylation at CD28 site Y209, indicating that another mechanism, such as the folding of the CD3ζ protein chain, must contribute to the increased phosphorylation at this particular site. The results also predict that this increase in the C2 site phosphorylation kinetics could allow CD3ζ on the 28ζ CAR protein to become fully phosphorylated at a lower signaling threshold, potentially adding to the stronger T cell activation of the 28ζ CAR compared to CD3ζ alone.

Taken together, this work provides new insights into the activation of CAR-T cells through quantitative phospho-proteomic experiment and computational modeling. Our model predicts how the separate actions of protein binding and catalytic activity influence CD3ζ ITAM phosphorylation. In addition to producing novel measurements and a modeling framework that explains experimental observations, our work generates new hypotheses regarding protein phosphorylation that can be applied to better engineer CARs that more optimally activate T cells for therapeutic purposes.

Author Contributions

J.A.R., P.W. and S.D.F. conceived and designed the project. J.A.R. performed the experiments, advised by P.W. D.Z. acquired the phospho-proteomic data, advised by N.A.G. J.A.R. analyzed the proteomic data, advised by N.A.G. J.A.R performed the computational modeling, advised by S.D.F. J.A.R. wrote the original draft. All co-authors contributed in reviewing and editing the manuscript. J.A.R, N.A.G, P.W. and S.D.F. provided funding and resources to support the project.

Acknowledgements

The authors would like to thank the lab of Ronald Vale at UCSF for providing the recombinant protein plasmids. This work was supported by the National Cancer Institute of the National Institutes of Health under Award Numbers F31CA200242 (to J.A.R.), R01EB017206, R01CA170820, and P01CA132681 (to P.W.)

Conflicts of Interest

The authors have no conflicts of interest to disclose.

Methods

Recombinant protein expression and purification

His_{10}-KKCK-CD3ζ in the pET28a vector and HIS_{10}-LCK-G2A in the pFastBacHTA vector were a kind gift from Dr. Ronald Vale (Hui & Vale, 2014). To make the HIS_{10}-CD28-CD3ζ recombinant protein, the DNA sequence for the intracellular domain of CD28 (aa 180-220) was codon optimized and constructed by Integrated DNA Technologies (IDT-DNA). This sequence was then cloned directly upstream of CD3ζ in the pET28a vector using Gibson assembly. All individual point mutations in the CAR vectors were introduced by the QuikChange XL site-directed mutagenesis kit (Agilent).

The sequence for HIS_{10}-LCK-G2A was amplified out of the pFastBacHTA vector by PCR and cloned into the FUW vector through Gibson assembly. LCK is able to undergo autophosphorylation at both activating and inhibitory tyrosine sites (Y394 and Y505, respectively). We previously showed that when LCK is phosphorylated at these tyrosine residues, it has differential catalytic activity (Rohrs *et al*, 2016). Therefore, to exclude any confounding effects due to changes in enzymatic efficiency, we used a constitutively active form of LCK containing a tyrosine to phenylalanine mutation at the inhibitory site (Y505F). This point mutation was introduced by the QuikChange XL site-directed mutagenesis kit (Agilent).

All CAR proteins were expressed in the BL28(DE3) strain of E. coli cells. E. coli cells were lysed as described in (Li *et al*, 2010). His_{10}-LCK-G2A-Y505F was transiently expressed in HEK293T cells through a standard calcium phosphate precipitation protocol (Pear *et al*, 1993). 48 hours after transfection, HEK293T cells were lysed in buffer containing 20 mM Tris·HCl, pH 7.5, 600 mM NaCl, 2 mM MgCl2, 5 mM immidazole, 10% glycerol, 1% NP-40, 1 mM Na3VO4, 10 mM NaF, and 1× complete protease inhibitor (Roche)). All HIS_{10} proteins were purified using FPLC, first on a Ni-NTA agarose column followed by gel purification using the HiPrep 16/60 Sephacryl S-200 HR column (GE Life Sciences) in HEPES-buffered saline (HBS) solution containing 50 mM HEPES-NaOH (pH 7.5), 150 mM NaCl, and 10% glycerol, as described in (Hui & Vale, 2014). Protein monomer fractions were concentrated, snap frozen in liquid nitrogen, and stored at −80°C. All purified recombinant proteins were quantified by SDS-PAGE and Coomassie staining using BSA as a standard.

Mass spectrometry confirmed that nearly 100% of the purified LCK-Y505 is phosphorylated at the activating Y394 site, while 100% of the CAR proteins were unphosphorylated after purification.

Liposome preparation

Synthetic 1,2-dioleoyl-sn-glycero-3-phosphocholine (POPC), 1-palmitoyl-2-oleoyl-sn-glycero-3-phospho-l-serine (POPS), and 1,2-dioleoyl-sn-glycero-3-[(N-(5-amino-1-carboxypentyl)iminodiacetic acid)succinyl] (nickel salt, DGS-NTA-Ni) were purchased from Avanti Polar Lipids and resuspended in chloroform. Liposomes were prepared as described in (Hui & Vale, 2014). Briefly, phospholipids (80% POPC, 10% POPS, 10% DGS-NTA-Ni) were dried as thin films under Ar gas and desiccated overnight. The lipids were then resuspended in 1x kinase buffer (50 mM HEPES-NaOH (pH 7.5), 150 mM NaCl, 10 mM MgCl2, 1 mM TCEP), and subjected to 5x freeze thaw cycles. The lipid mixture was then extruded through 200 nm pore-size polycarbonate filters to produce large unilamellar liposomes. For liposomes with varying POPS concentration, the amount was compensated for by adjusting the POPC concentration.

Protein phosphorylation time courses
HIS-tagged LCK and CAR proteins were mixed with Ni-bearing liposomes for 1 hour to allow for the proteins to attach to nickel bearing lipids on the surface of the liposome, as calculated and described in (Hui & Vale, 2014). We used 20,000 molecules/μm^2 CAR proteins and titrated down LCK to a very low concentration to allow us to distinguish the differences between the CD3ζ site phosphorylation kinetics. Estimation of the final LCK concentration is described in the *Mechanistic computational modeling* section. Once the proteins attached to the liposomes, 10x ATP in kinase buffer was added to a final concentration of 1M. Samples were taken at various times and the reaction was stopped by adding urea to 8M and boiling for 5 minutes. Time samples were then frozen at -20°C until they were prepared for phospho-proteomic mass spectrometry.

Standard curve preparation
As different peptides will travel through the mass spectrometer with different efficiencies resulting in different MS intensities for the same amount of peptide, a standard curve is necessary to compare between peptide MS intestines in a sample. We constructed our standard curves based on a known ratio of phosphorylated:unphosphorylated peptide. For each CAR protein, we quantified the amount of protein and aliquoted the same volume from a given sample into two vials. To one vial we added LCK and ATP and let LCK phosphorylate the CAR overnight. To the other vial, we added equal volumes of HBS buffer, so that the phosphorylated and unphosphorylated CAR proteins would remain at the same concentration. The next morning, urea was added to both vials to a final concentration of 8M. We then combined various volume ratios of the two solutions to create a standard curve with known ratios of phosphorylated:unphosphorylated peptides. The standard curve samples were then stored at -20°C until they were ready to be prepared for analysis by mass spec.

Phospho-proteomic sample preparation
The time course samples were thawed to room temperature and reduced by the addition of DTT to a final concentration of 5 mM for 1 hr at 37°C. Samples were next alkylated with iodoacetamide at a final concentration of 25 mM for 1 hr at room temperature in the dark. This reaction was quenched by the addition of DTT to a final concentration of 10 mM for 30 min. Samples were then diluted to a final urea concentration of 2 M with 100 mM Tris, pH 8, and trypsin digested overnight at 37°C. The next morning, samples were acidified to a pH<4 with 5% TFA, purified by C18 zip-tip (Millipore) according to the manufacturer's instructions, and eluted into 50% acetonitrile solution. Purified samples were then dried and stored at -80°C until they were ready to be analyzed.

Phospho-proteomic data collection
All data samples were run in technical duplicates. Data was run in three sets, each with their own standard curve, shown in **Supplemental Figure S1**: (1) first biological replicate of the wild type ITAM phosphorylation on 10% POPS liposomes, the wild type ITAM phosphorylation on 0% and 45% POPS liposomes, and a CD3ζ standard curve, (2) the second biological replicate of the wild type ITAM phosphorylation on 10% POPS liposomes, the individual tyrosine to phenylalanine CD3ζ ITAM point mutants, and a CD3ζ standard curve, (3) all 28ζ proteins, including the Y206F and Y209F mutants, and a standard curve for 28ζ, CD28-Y206F-CD3ζ, and CD28-Y209F-CD3ζ. Desalted samples were reconstituted in buffer A (0.1% formic acid). The samples were injected into an Easy 1200 nanoLC untra-high pressure liquid chromatography coupled to a Q-Exactive Plus mass spectrometer (Thermo Fisher Scientific). Peptides were separated

by reversed-phase chromatography (PepMap RSLC C18, 2µm, 100Å, 75 µm X 15 cm). The flow rate was set to 300 nl/min at a gradient starting with 6% buffer B (0.1% FA, 80% acetonitrile) to 55% B in 25 minutes, followed by an 8 minutes washing step to 100% B. The maximum pressure was set to 1180 bar and column temperature was constant at 50 ˚C.

Peptides separated by the column were ionized at 2.0 kV in the positive ion mode. MS1 survey scans were acquired at resolution of 70k from 275 to 1500 m/z, with maximum injection time of 80 ms and AGC target of 1e6. MS/MS fragmentation of the 10 most abundant ions were analyzed at a resolution of 35k, AGC target 1e5, maximum injection time 100 ms, and normalized collision energy 25. Dynamic exclusion was set to 10 s and ions with charge 1, 7, and >7 were excluded.

Mass spec data analysis and normalization

MS/MS fragmentation spectra were searched with Proteome Discoverer SEQUEST (version 1.4, Thermo Scientific) against the in-silico tryptic digested recombinant protein sequences (17 entries) used in this study. The maximum missed cleavages was set to 2. Dynamic modifications were set to oxidation on methionine, phosphorylation on serine, threonine, and tyrosine, and acetylation on protein N-terminus. Fixed modification was set to carbamidomethylation on cysteine residues. The maximum parental mass error was set to 10 ppm and the MSMS mass tolerance was set to 0.02 Da. False Discovery threshold was set to 0.01 using Percolator node validated by q-value. Phosphosite localization probability was calculated using PhosphoRS node.

MS1 peak quantification was performed manually in Skyline (version 3.7) for each phosphorylated/unphosphorylated peptide pair. We analyzed only peptides with no missed cleavages and no modifications besides tyrosine phosphorylation, which were consistently the largest peaks. One exception was made for the CD28 peptide containing tyrosine site Y218. The unphosphorylated form of this peptide was smaller than the cutoff mass to charge ratio used in our data collection. Therefore, we analyzed this site using the peptide with one N-terminal missed cleavage.

To create our peptide standard curves, we calculated the ratio of each phosphorylated/unphosphorylated peptide, plotted them against the known ratios and fit the resulting linear plots (**Supplemental Figure S1**). Technical replicates of each peptide were combined together to fit the standard curves so that one standard curve was used to normalize the phosphorylated/unphosphorylated peptide intensity ratios for each set of peptide time course technical replicates. We then used the normalized ratios to calculate the percent phosphorylation over time for each time course technical replicate and used the two sets to calculate the mean and standard deviation of the data. Time courses were only normalized to the standard curve data collected at the same time.

Statistical analysis

All statistical analyses were done using a one-way ANOVA followed by multiple pair-wise comparisons using the Tukey t-test in Prism (version 7, GraphPad)

Sigmoidal parameter calculations

Data was fit in Prism (version 7, GraphPad) to a standard sigmoidal curve with plateaus at 0 and 100%.

$$y = \frac{100}{1+10^{(\log(t_{half})-x)*Hill}} \quad (1)$$

Where x is the time on a log scale, y is the output, t_{half} is the half maximal time, and *Hill* is the Hill coefficient. For the comparison of t_{half} and *Hill* for the random and sequential models, the models were first fit to data using MATLAB, as described in the "Mechanistic computational modeling" section below. The model responses were then entered into Prism as data sets and fit to Equation 1.

Mechanistic computational modeling

Our mechanistic computational model was written as a set of rules in BioNetGen (Faeder *et al*, 2009) and implemented in MATLAB (**Supplemental Files S1 and S2**). We used mass action kinetics to describe the association, dissociation, and catalytic activity of LCK for each of the six ITAM sites. The parameters were fit to the data using particle swarm optimization (PSO) (Iadevaia *et al*, 2010). Each data set was fit 50 times to get a range of parameter values. From these parameter values, the substrate specificity (SS) of LCK for each of the six sites was calculated as described in Equation 2:

$$SS = \frac{k_{cat}}{K_M} = \frac{k_{cat} \cdot k_{on}}{k_{off}+k_{cat}} \quad (2)$$

Where SS is substrate specificity, k_{cat} is the catalytic rate, K_M is the Michaelis-Menten constant, k_{on} is the association rate, and k_{off} is the dissociation rate.

The initial conditions for the CAR proteins were based on the measured protein densities used in the experiments, 20,000 molecules/μm^2. In order to be able to distinguish between the phosphorylation kinetics of CAR tyrosine sites, very low concentrations of LCK were used in the experiments. This experimental condition also agrees with the assumption of Michaelis-Menten kinetics that the enzyme concentration is much less than the substrate concentration, allowing us to use the K_M value in our calculation of substrate specificity. However, this low level of LCK made it very difficult to measure the exact concentration relative to the experimental errors. Therefore, we used the calculated Michaelis-Menten parameters for LCK phosphorylation of CD3ζ from (Hui & Vale, 2014) to estimate a more exact initial concentration of LCK. We first took our site-specific data and calculated the average total CD3ζ phosphorylation over time. We then made a CD3ζ phosphorylation model using Michaelis-Menten kinetics and the parameters from (Hui & Vale, 2014), and fit the concentration of LCK to the data. An average of approximately 1 molecule/μm^2 fit the data best and was, therefore, used to fit our site-specific parameters (**Supplemental Figure S6**).

To explore the emergence of the 21 kDa form of CD3ζ, we extended the model to account for doubly phosphorylated ITAMs (**Supplemental File S3**). We combined the ITAM tyrosine site pairs onto the same molecule (ITAM A: A1+A2, ITAM B: B1+B2, ITAM C: C1+C2), keeping the LCK phosphorylation kinetic parameters consistent along the contour lines shown in **Figure 3A** based on the initial fits listed in **Supplemental Table S1**. A generic first order dephosphorylation mechanism was employed to account for a variety of different phosphatases present in the T cells. As LCK and most phosphatases (specifically CD45) are large molecules compared to the CD3ζ ITAMs, in the model, the phosphatase can only act on ITAMs without LCK bound at either tyrosine site. ZAP-70 contained two binding sites that could bind only to doubly phosphorylated ITAMs. We used this model to explore a wide range of parameter values.

References

Aivazian D & Stern LJ (2000) Phosphorylation of T cell receptor zeta is regulated by a lipid dependent folding transition. *Nat. Struct. Biol.* **7:** 1023–6 Available at: http://www.ncbi.nlm.nih.gov/pubmed/11062556

Au-Yeung BB, Deindl S, Hsu L-Y, Palacios EH, Levin SE, Kuriyan J & Weiss A (2009) The structure, regulation, and function of ZAP-70. *Immunol. Rev.* **228:** 41–57 Available at: http://www.ncbi.nlm.nih.gov/pubmed/19290920

Boomer JS & Green JM (2010) An enigmatic tail of CD28 signaling. *Cold Spring Harb. Perspect. Biol.* **2:** a002436 Available at: http://www.pubmedcentral.nih.gov/articlerender.fcgi?artid=2908766&tool=pmcentrez&rendertype=abstract [Accessed April 11, 2014]

Bu J, Shaw AS & U ACC (1995) Analysis of then interaction of Zap-70 and Syk protein-tyrosine kinases with the T cell antigen receptor by plasmon resonance. **92:** 5106–5110

Carey KD, Dillon TJ, Schmitt JM, Baird a M, Holdorf a D, Straus DB, Shaw a S & Stork PJ (2000) CD28 and the tyrosine kinase lck stimulate mitogen-activated protein kinase activity in T cells via inhibition of the small G protein Rap1. *Mol. Cell. Biol.* **20:** 8409–8419

Chae W-J, Lee H-K, Han J-H, Kim S-WV, Bothwell ALM, Morio T & Lee S-K (2004) Qualitatively differential regulation of T cell activation and apoptosis by T cell receptor zeta chain ITAMs and their tyrosine residues. *Int. Immunol.* **16:** 1225–1236

Chakraborty AK & Weiss A (2014) Insights into the initiation of TCR signaling. *Nat. Immunol.* **15Chakrabo:** 798–807 Available at: http://www.nature.com/ni/journal/v15/n9/abs/ni.2940.html#affil-auth [Accessed July 29, 2015]

Dobbins J, Gagnon E, Godec J, Pyrdol J, Vignali DAA, Sharpe AH & Wucherpfennig KW (2016) Binding of the cytoplasmic domain of CD28 to the plasma membrane inhibits Lck recruitment and signaling. **9:** 1–13

Faeder JR, Blinov ML & Hlavacek WS (2009) Rule-based modeling of biochemical systems with BioNetGen. *Methods Mol. Biol.* **500:** 113–67 Available at: http://www.ncbi.nlm.nih.gov/pubmed/19399430

Fesnak AD, June CH & Levine BL (2016) Engineered T cells: The promise and challenges of cancer immunotherapy. *Nat. Rev. Cancer* **16:** 566–581 Available at: http://dx.doi.org/10.1038/nrc.2016.97

Firor AE, Jares A & Ma Y (2015) From humble beginnings to success in the clinic: Chimeric antigen receptor-modified T-cells and implications for immunotherapy. *Exp. Biol. Med.* **240:** 1087–1098

Gagnon E, Schubert D a, Gordo S, Chu HH & Wucherpfennig KW (2012) Local changes in lipid environment of TCR microclusters regulate membrane binding by the CD3ε cytoplasmic domain. *J. Exp. Med.* **209:** 2423–39 Available at: http://www.pubmedcentral.nih.gov/articlerender.fcgi?artid=3526357&tool=pmcentrez&rendertype=abstract

Harris DT, Hager M V, Smith SN, Stone JD, Kruger P, Lever M, Schmitt TM, Greenberg PD, Kranz M, Kruger P, Lever M, Dushek O, Schmitt TM & Greenberg PD (2018) Comparison of T Cell Activities Mediated by Human TCRs and CARs That Use the Same Recognition Domains. *J. Immunol.*

Hofinger E & Sticht H (2005) Multiple modes of interaction between Lck and CD28. *J. Immunol.* **174:** 3839–3840; author reply 3840 Available at: http://www.jimmunol.org/content/174/7/3839.2.full

Holdorf AD, Lee K-H, Burack WR, Allen PM & Shaw AS (2002) Regulation of Lck activity

by CD4 and CD28 in the immunological synapse. *Nat. Immunol.* **3:** 259–64 Available at: http://www.ncbi.nlm.nih.gov/pubmed/11828322 [Accessed January 27, 2014]

Housden HR, Skipp PJS, Crump MP, Broadbridge RJ, Crabbe T, Perry MJ & Gore MG (2003) Investigation of the kinetics and order of tyrosine phosphorylation in the T-cell receptor zeta chain by the protein tyrosine kinase Lck. *Eur. J. Biochem.* **270:** 2369–2376

Hui E, Cheung J, Zhu J, Su X, Taylor MJ, Wallweber HA, Sasmal DK, Huang J, Kim JM, Mellman I & Vale RD (2017) T cell costimulatory receptor CD28 is a primary target for PD-1–mediated inhibition. *Science (80-.).* **4:** eaaf1292 Available at: http://www.sciencemag.org/lookup/doi/10.1126/science.aaf1292

Hui E & Vale RD (2014) In vitro membrane reconstitution of the T-cell receptor proximal signaling network. *Nat. Struct. Mol. Biol.* **21:** 133–42 Available at: http://www.ncbi.nlm.nih.gov/pubmed/24463463 [Accessed March 21, 2014]

Iadevaia S, Lu Y, Morales FC, Mills GB & Ram PT (2010) Identification of optimal drug combinations targeting cellular networks: integrating phospho-proteomics and computational network analysis. *Cancer Res.* **70:** 6704–14 Available at: http://www.pubmedcentral.nih.gov/articlerender.fcgi?artid=2932856&tool=pmcentrez&rendertype=abstract [Accessed November 12, 2014]

Ilani T, Khanna C, Zhou M, Veenstra TD & Bretscher A (2007) Immune synapse formation requires ZAP-70 recruitment by ezrin and CD43 removal by moesin. *J. Cell Biol.* **179:** 733–746

Jenkins MR, Stinchcombe JC, Au-Yeung BB, Asano Y, Ritter AT, Weiss A & Griffiths GM (2014) Distinct structural and catalytic roles for Zap70 in formation of the immunological synapse in CTL. *Elife* **2014:** 1–21

Kersh BEN, Kersh GJ & Allen PM (1999) Partially Phosphorylated T Cell Receptor Zeta Molecules Can Inhibit Inhibit T Cell Activation. **190:**

Kersh EN (1998) Fidelity of T Cell Activation Through Multistep T Cell Receptor Phosphorylation. *Science (80-.).* **281:** 572–575 Available at: http://www.sciencemag.org/cgi/doi/10.1126/science.281.5376.572 [Accessed March 8, 2014]

Kingwell K (2017) CAR T therapies drive into new terrain. *Nat. Rev. Drug Discov.* **16:** 301–304 Available at: http://dx.doi.org/10.1038/nrd.2017.84

Lee DW, Kochenderfer JN, Stetler-Stevenson M, Cui YK, Delbrook C, Feldman SA, Fry TJ, Orentas R, Sabatino M, Shah NN, Steinberg SM, Stroncek D, Tschernia N, Yuan C, Zhang H, Zhang L, Rosenberg SA, Wayne AS & Mackall CL (2015) T cells expressing CD19 chimeric antigen receptors for acute lymphoblastic leukaemia in children and young adults: A phase 1 dose-escalation trial. *Lancet* **385:** 517–528 Available at: http://dx.doi.org/10.1016/S0140-6736(14)61403-3

Lee KA, Craven KB, Niemi GA & Hurley JB (2002) Mass spectrometric analysis of the kinetics of in vivo rhodopsin phosphorylation. *Protein Sci* **11:** 862–874 Available at: http://www.ncbi.nlm.nih.gov/pubmed/11910029%5Cnhttp://onlinelibrary.wiley.com/store/10.1110/ps.3870102/asset/110862_ftp.pdf?v=1&t=i7vm0sqx&s=342f456a0d9137f5b52b88a9dd0041bb3b7b8668

Leupin O, Zaru R, Laroche T, Müller S & Valitutti S (2000) Exclusion of CD45 from the T-cell receptor signaling area in antigen-stimulated T lymphocytes. *Curr. Biol.* **10:** 277–280

Li H, Korennykh a V, Behrman SL & Walter P (2010) Mammalian endoplasmic reticulum stress sensor IRE1 signals by dynamic clustering. *Proc Natl Acad Sci U S A* **107:** 16113–16118 Available at: http://www.ncbi.nlm.nih.gov/pubmed/20798350

Lovatt M, Filby A, Parravicini V, Werlen G, Palmer E & Zamoyska R (2006) Lck

Regulates the Threshold of Activation in Primary T Cells, While both Lck and Fyn Contribute to the Magnitude of the Extracellular Signal-Related Kinase Response. *Mol. Cell. Biol.* **26:** 8655–8665 Available at: http://mcb.asm.org/cgi/doi/10.1128/MCB.00168-06

Lu Y, Phillips C a, Bjorndahl JM & Trevillyan JM (1994) CD28 signal transduction: tyrosine phosphorylation and receptor association of phosphoinositide-3 kinase correlate with Ca(2+)-independent costimulatory activity. *Eur. J. Immunol.* **24:** 2732–9 Available at: http://www.ncbi.nlm.nih.gov/pubmed/7957566

Michel F, Attal-Bonnefoy G, Mangino G, Mise-Omata S & Acuto O (2001) CD28 as a molecular amplifier extending TCR ligation and signaling capabilities. *Immunity* **15:** 935–45 Available at: http://www.ncbi.nlm.nih.gov/pubmed/11754815

Moon EK, Wang LC, Dolfi D V., Wilson CB, Ranganathan R, Sun J, Kapoor V, Scholler J, Puré E, Milone MC, June CH, Riley JL, Wherry EJ & Albelda SM (2014) Multifactorial T-cell hypofunction that is reversible can limit the efficacy of chimeric antigen receptor-transduced human T cells in solid tumors. *Clin. Cancer Res.* **20:** 4262–4273

Morgan RA, Yang JC, Kitano M, Dudley ME, Laurencot CM & Rosenberg SA (2010) Case report of a serious adverse event following the administration of t cells transduced with a chimeric antigen receptor recognizing ERBB2. *Mol. Ther.* **18:** 843–851 Available at: http://dx.doi.org/10.1038/mt.2010.24

Mukhopadhyay H, Wet B De, Clemens L, Maini PK, Allard J, van der Merwe PA & Dushek O (2016) Multisite phosphorylation of the T cell receptor ⇣-chain modulates potency but not the switch-like response. *Biophys. J.* **110:** 1896–1906 Available at: http://dx.doi.org/10.1016/j.bpj.2016.03.024

Mullard A (2017) Second anticancer CAR T therapy receives FDA approval. *Nat. Rev. Drug Discov.* **16:** 818–818 Available at: http://www.nature.com/doifinder/10.1038/nrd.2017.249

Nika K, Soldani C, Salek M, Paster W, Gray A, Etzensperger R, Fugger L, Polzella P, Cerundolo V, Dushek O, Höfer T, Viola A & Acuto O (2010) Constitutively active Lck kinase in T cells drives antigen receptor signal transduction. *Immunity* **32:** 766–77 Available at: http://www.pubmedcentral.nih.gov/articlerender.fcgi?artid=2996607&tool=pmcentrez&rendertype=abstract [Accessed March 17, 2014]

van Oers NS, Tohlen B, Malissen B, Moomaw CR, Afendis S & Slaughter C a (2000) The 21- and 23-kD forms of TCR zeta are generated by specific ITAM phosphorylations. *Nat. Immunol.* **1:** 322–8 Available at: http://www.ncbi.nlm.nih.gov/pubmed/11017104

Palacios EH & Weiss A (2004) Function of the Src-family kinases, Lck and Fyn, in T-cell development and activation. *Oncogene* **23:** 7990–8000

Pear WS, Nolan GP, Scott ML & Baltimore D (1993) Production of high-titer helper-free retroviruses by transient transfection (retroviral packaing cells/gene therapy). *Cell Biol.* **90:** 8392–8396

Pitcher L a, Young J a, Mathis M a, Wrage PC, Bartók B & van Oers NSC (2003) The formation and functions of the 21- and 23-kDa tyrosine-phosphorylated TCR zeta subunits. *Immunol. Rev.* **191:** 47–61

Rohrs JA, Wang P & Finley SD (2016) Predictive Model of Lymphocyte-Specific Protein Tyrosine Kinase (LCK) Autoregulation. *Cell. Mol. Bioeng.* **9:** 351–367

Schlosshauer M & Baker D (2004) Realistic protein-protein association rates from a simple diffusional model neglecting long-range interactions, free energy barriers, and landscape ruggedness. *Protein Sci.* **13:** 1660–1669

Sjölin-goodfellow H, Frushicheva MP, Ji Q, Cheng DA, Kadlecek TA, Cantor AJ &

Kuriyan J (2015) The catalytic activity of the kinase ZAP-70 mediates basal signaling and negative feedback of the T cell receptor pathway. **8:** 1–14

Stanford SM, Rapini N & Bottini N (2012) Regulation of TCR signalling by tyrosine phosphatases: From immune homeostasis to autoimmunity. *Immunology* **137:** 1–19

Teng JM, King PD, Sadra A, Liu X, Han A, Selvakumar A, August A & Dupont B (1996) Phosphorylation of each of the distal three tyrosines of the CD28 cytoplasmic tail is required for CD28-induced T cell IL-2 secretion. *Tissue Antigens* **48:** 255–264 Available at: http://www.ncbi.nlm.nih.gov/entrez/query.fcgi?cmd=Retrieve&db=PubMed&dopt=Citation&list_uids=8946678

Tian R, Wang H, Gish GD, Petsalaki E, Pasculescu A, Shi Y, Mollenauer M, Bagshaw RD, Yosef N, Hunter T, Gingras AC, Weiss A & Pawson T (2015) Combinatorial proteomic analysis of intercellular signaling applied to the CD28 T-cell costimulatory receptor. *Proc Natl Acad Sci U S A* **112:** E1594-603 Available at: http://www.ncbi.nlm.nih.gov/pubmed/25829543

Figures

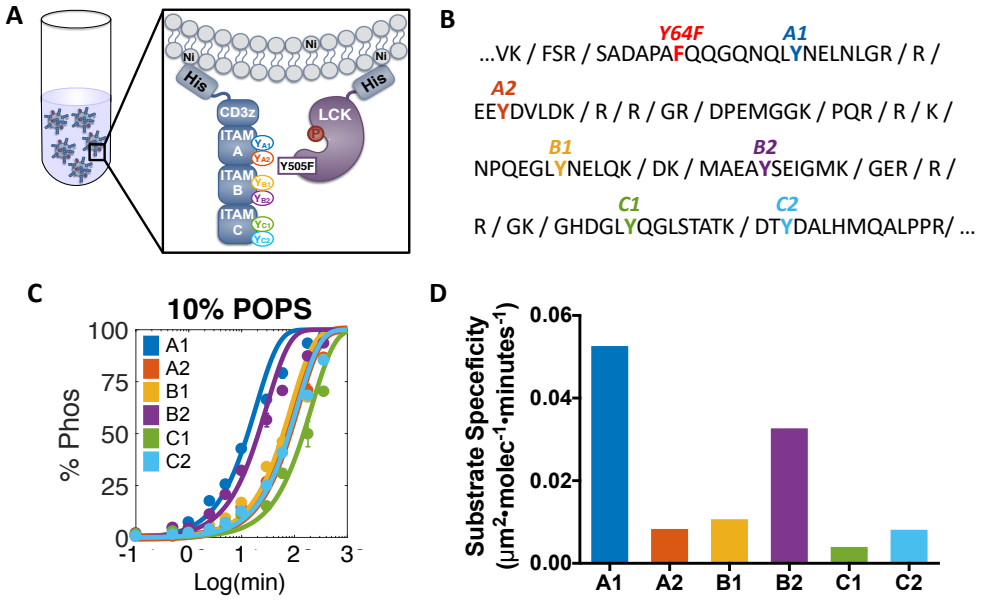

Figure 1: CD3ζ sites are phosphorylated by LCK randomly with different kinetics.

(A) Schematic of the experimental liposomal system. CD3ζ and LCK his-tagged proteins were purified and allowed to bind to large unilamellar liposomes bearing nickel-chelated lipids. Once proteins were bound, ATP was added, and the proteins were allowed to interact for various times before being subjected to phospho-proteomic mass spectrometry for quantification.

(B) Sequence of CD3ζ intracellular domain with trypsin cut sites denoted. Individual ITAM tyrosine sites are labeled in different colors. Y64F indicates a tyrosine to phenylalanine mutation to ensure that each peptide only has one tyrosine phosphorylation site.

(C) Experimental data (dots) and model fit (lines) for CD3ζ ITAM phosphorylation on liposomes containing 10% acidic POPS lipids. Error bars represent the standard deviation of two technical replicates normalized by site-specific standard curves.

(D) Substrate specificity of individual CD3ζ ITAM sites, as calculated from the model fit parameters. 50 rounds of model fitting gave nearly identical calculations of substrate specificities.

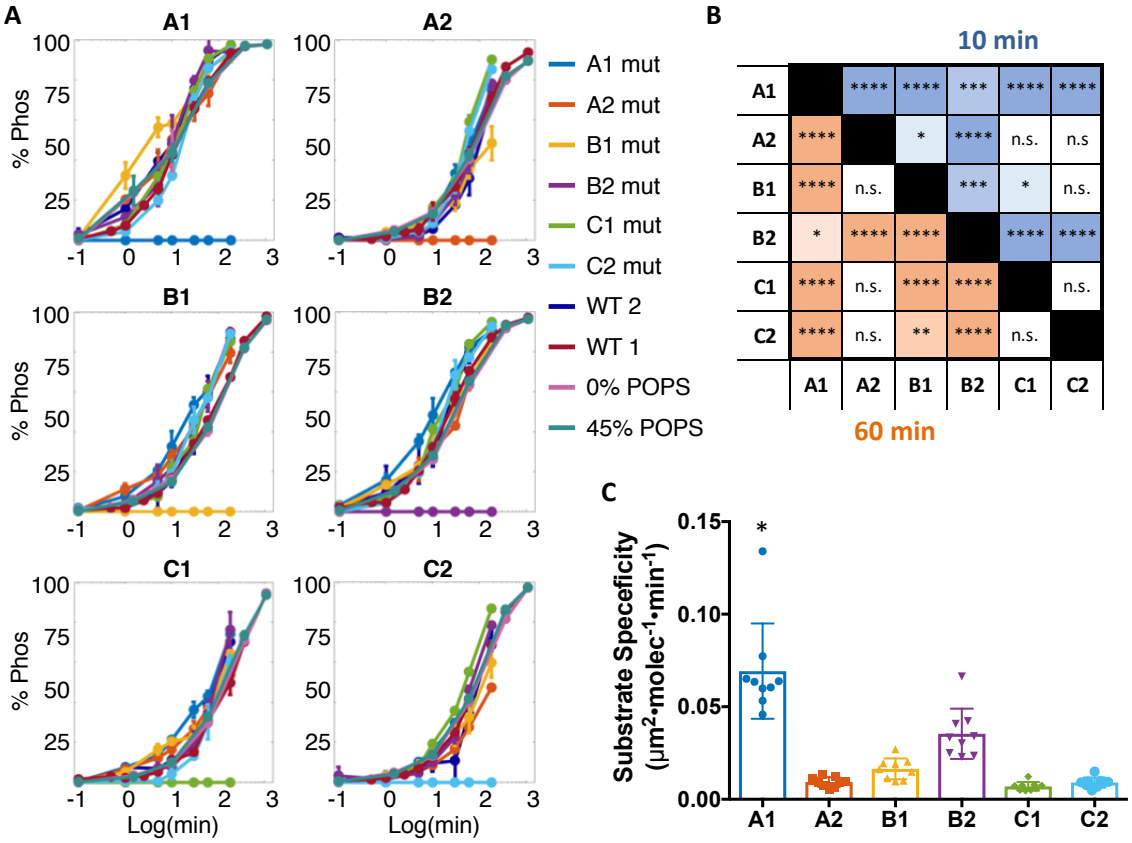

Figure 2: The individual tyrosine sites do not influence the phosphorylation kinetics of each other.

(A) Experimental data for each CD3ζ ITAM site for different experimental conditions: WT 1 and 2 - biological replicates of CD3ζ with unmutated ITAMs on liposomes containing 10% POPS, XX mut (where XX represents the tyrosine to phenylalanine ITAM mutation site for CD3ζ stimulated on 10% POPS liposomes), and X% PS (where X represents the POPS concentration for liposomes bearing CD3ζ with wild type ITAMs). Error bars represent the standard deviation of two technical replicates normalized by site-specific standard curves.

(B) Statistical comparison of CD3ζ ITAM site phosphorylation levels at 10 (blue) and 60 (orange) minutes as measured by pairwise Tukey t-tests (**** $p<0.0001$, *** $p<0.001$, ** $p<0.01$, * $p<0.05$, n.s. not significant).

(C) Substrate specificity of individual CD3ζ ITAM sites. Bars represent the mean and standard deviation as calculated from the model fits in Figure 1A and Supplemental Figure S4. Stars indicate sites that are statistically different from all other sites (* $p<0.05$).

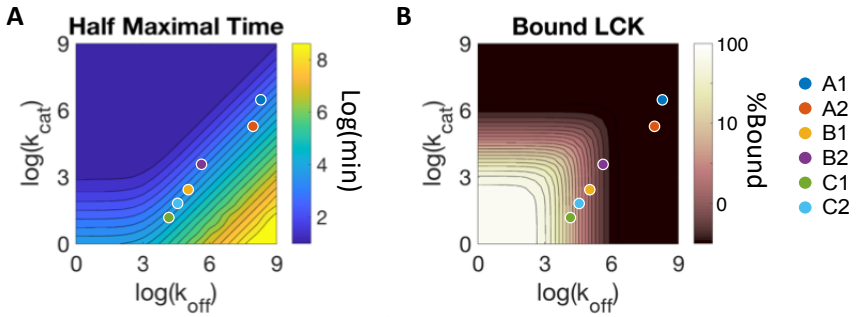

Figure 3: CD3ζ phosphorylation is consistent across a range of LCK binding and catalytic rates.

(A) Heat map of the half maximal time estimated from the predicted phosphorylation time course as a function of varying LCK dissociation rate (x-axis) and catalytic rate (y-axis). The chosen baseline model fit parameters for each ITAM site are indicated by the dots.

(B) Heat map of maximal LCK binding as a function of dissociation rate (x-axis) and catalytic rate (y-axis). The chosen model fit parameters for each ITAM site are indicated by the dots.

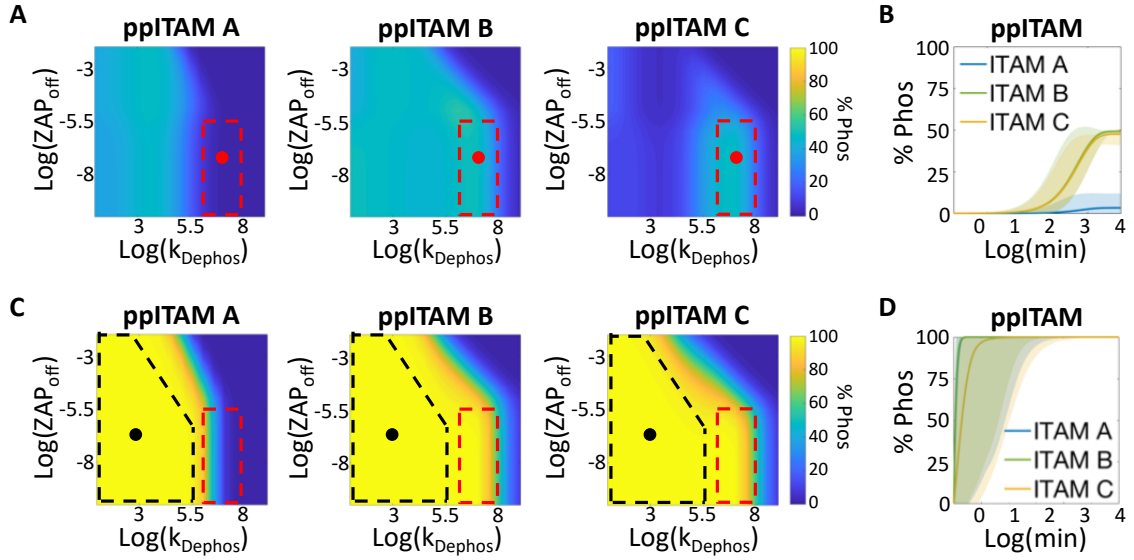

Figure 4: A range of ZAP-70 binding parameters and phosphatase activities lead to the formation of the 21 kDa partially phosphorylated form of CD3ζ.

(A) Heat maps showing the percent of doubly phosphorylated CD3ζ ITAMs at steady state as a function of the dephosphorylation activity (x-axis) and ZAP-70 dissociation rate (y-axis) for initial conditions of 10,000 LCK/μm^2, 10,000 CD3ζ/μm^2, 10,000 ZAP-70/μm^2. The red dashed area indicates the parameter region in which ITAM A is significantly less phosphorylated than ITAMs B and C, representing the 21 kDa form of CD3ζ.

(B) Time course of ITAM phosphorylation. Lines are the model response for the parameters indicated by the red dot in (A), shaded regions are the 95% confidence interval of the model response for the parameters within the red dashed area of (A).

(C) Heat maps showing the percent of doubly phosphorylated CD3ζ ITAMs at steady state as a function of the dephosphorylation activity (x-axis) and ZAP-70 dissociation rate (y-axis) for initial conditions of 10,000 LCK/μm^2, 10,000 CD3ζ/μm^2, 30,000 ZAP-70/μm^2. The red dashed area indicates the parameter region in which ITAM A is significantly less phosphorylated than ITAMs B and C, representing the 21 kDa form of CD3ζ. The black dashed area indicates the parameter region in which all ITAMs are strongly phosphorylated at the same amount, representing the 23 kDa form of CD3ζ.

(D) Time course of ITAM phosphorylation. Lines are the model response for the parameters indicated by the black dot in (C), shaded regions are the 95% confidence interval of the model response for the parameters within the black dashed area of (C).

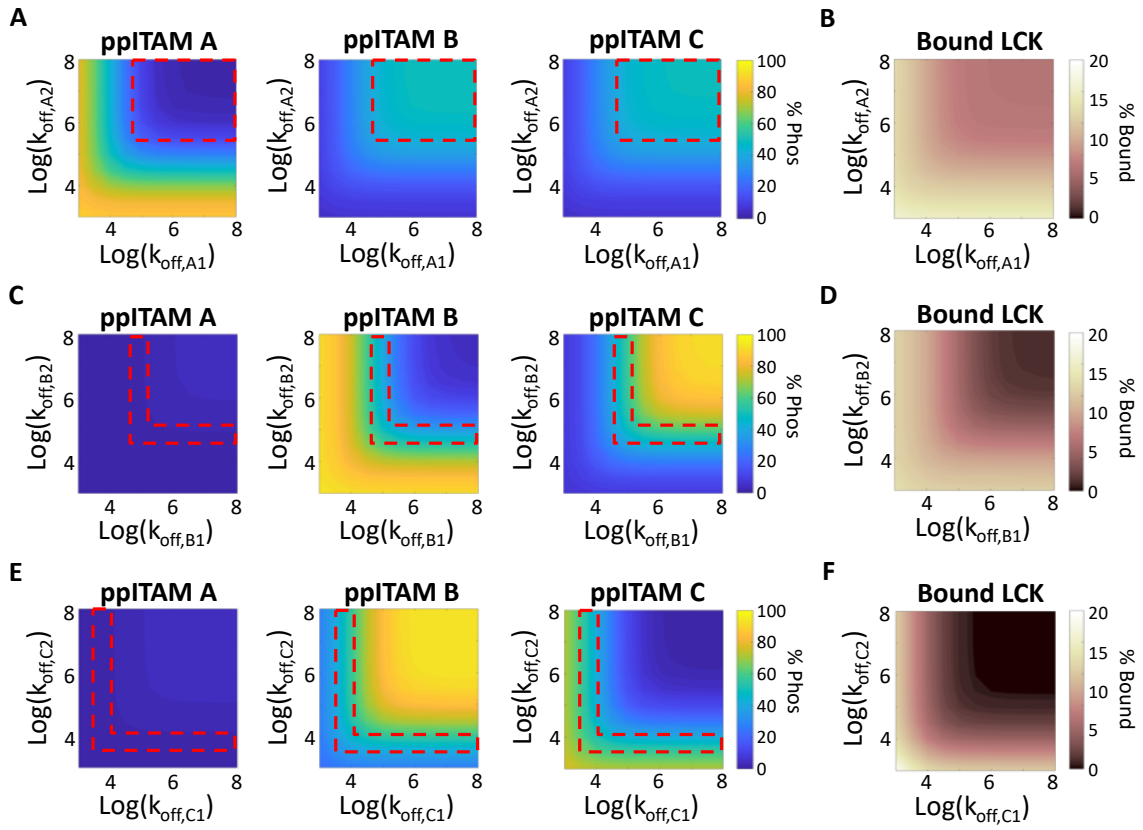

Figure 5: LCK binding and protection of partially phosphorylated ITAMs allows for slowly phosphorylated ITAM sites to reach higher steady state phosphorylation levels.

(A, C, E) Heat maps showing the model predictions for the percent of doubly phosphorylated CD3ζ ITAMs at steady state as a function of LCK binding for each of the two tyrosine sites on ITAM A (A), ITAM B (C), and ITAM C (E) with initial conditions of 10,000 LCK/μm^2, 10,000 CD3ζ/μm^2, 10,000 ZAP-70/μm^2. LCK binding was altered while maintaining the model fits shown in Figure 1 and Supplemental Figure S4 by changing the LCK dissociation and catalytic rates together along the contour lines shown in Figure 3. Red dashed areas indicate the parameter region in which ITAM A is significantly less phosphorylated than ITAMs B and C, representing the 21 kDa form of CD3ζ.

(B, D, F) Heat maps showing the maximum percent of bound LCK in the system at steady state as a function of LCK binding for each of the two tyrosine sites on ITAM A (B), ITAM B (D), or ITAM C (F).

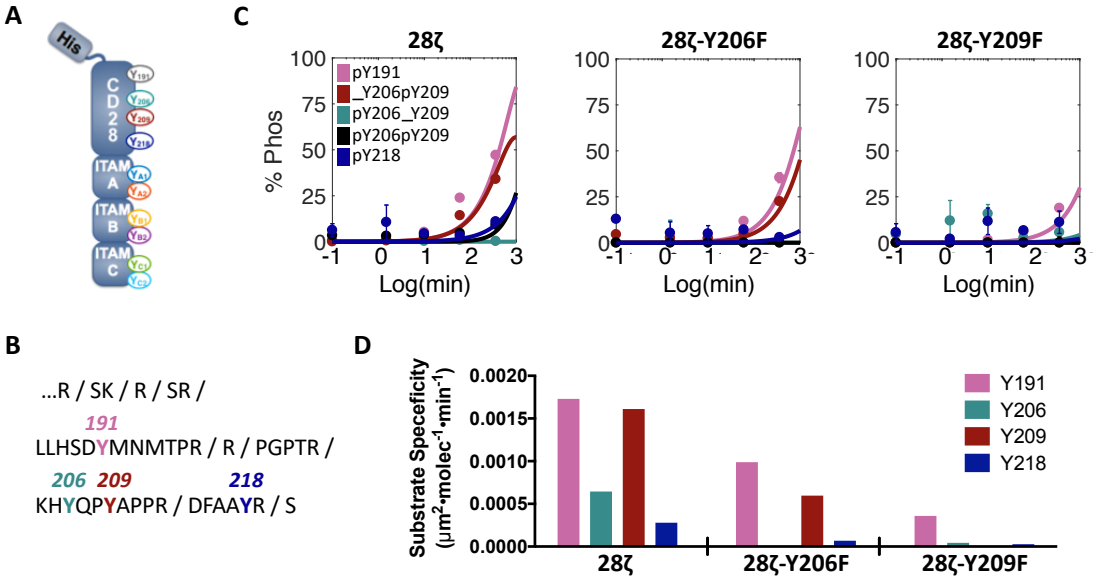

Figure 6: CD28 tyrosine sites are phosphorylated more slowly than CD3ζ tyrosine sites.

(A) Schematic of the His-tagged CD28-CD3ζ recombinant protein.

(B) Sequence of CD28 intracellular domain with trypsin cut sites denoted. Individual tyrosine sites are labeled in different colors.

(C) Experimental data (dots) and model fit (lines) for CD28 tyrosine site phosphorylation on wildtype CD28-CD3ζ, CD28-Y206F-CD3ζ, and CD28-Y209F-CD3ζ. Error bars represent the standard deviation of two technical replicates normalized by site-specific standard curves.

(D) Substrate specificity of individual CD28 tyrosine sites, as calculated from the model fits in (C). 50 rounds of model fitting gave nearly identical calculations of substrate specificities.

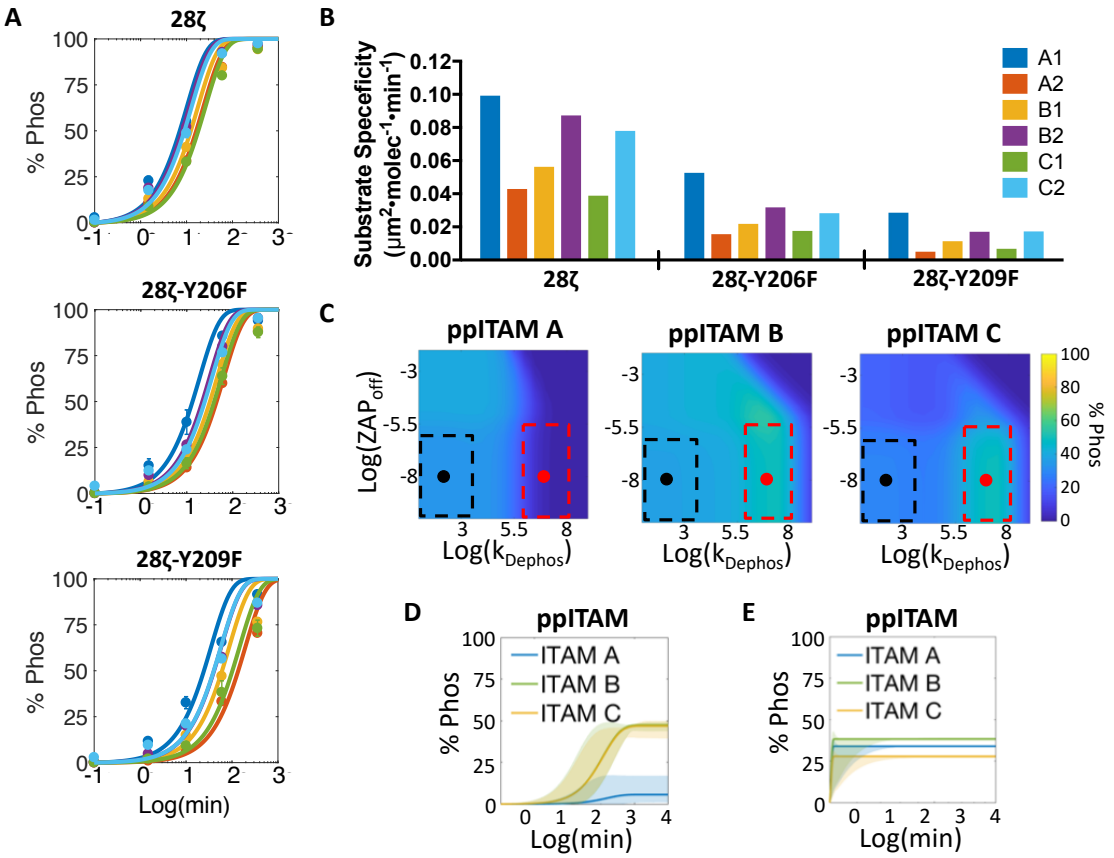

Figure 7: CD28 can affect the phosphorylation of CD3ζ sites

(A) Experimental data (dots) and model fit (lines) for CD3z ITAM phosphorylation on wildtype CD28-CD3ζ, CD28-Y206F-CD3ζ, and CD28-Y209F-CD3ζ. Error bars represent the standard deviation of two technical replicates normalized by site-specific standard curves.

(B) Substrate specificity of individual CD28 tyrosine sites as calculated from the model fits in (A). 50 rounds of model fitting gave nearly identical calculations of substrate specificities.

(C) Heat maps showing the percent of doubly phosphorylated CD3ζ ITAMs on the 28ζ protein at steady state as a function of the dephosphorylation activity (x-axis) and ZAP-70 dissociation rate (y-axis) for initial conditions of 10,000 LCK/μm^2, 10,000 CD3ζ/μm^2, 10,000 ZAP-70/μm^2. The red dashed area indicates the parameter region in which ITAM A is significantly less phosphorylated than ITAMs B and C, representing the 21 kDa form of CD3ζ. The black dashed area indicates the parameter region in which all ITAMs are phosphorylated at a similar level, representing the 23 kDa form of CD3ζ.

(D) Time course of 28ζ ITAM phosphorylation. Lines are the model response for the parameters indicated by the red dot in (C), shaded regions are the 95% confidence interval of the model response for the parameters within the red dashed area of (C).

(E) Time course of 28ζ ITAM phosphorylation. Lines are the model response for the parameters indicated by the black dot in (C), shaded regions are the 95% confidence interval of the model response for the parameters within the black dashed area of (C).

Supplement

Figure S1: Standard curves for phosphorylated:unphosphorylated peptide intensity normalization. Data was run on the mass spectrometer in three sets, and each set was normalized by a standard curve run at the same time. All of the standard curves used are shown here, with each row being used to analyze a separate set of data. Row 1 was used to analyze the first biological replicate of the wild type ITAM phosphorylation on 10% POPS liposomes and the wild type ITAM phosphorylation on 0% and 45% POPS liposomes. Row 2 was used to analyze the second biological replicate of the wild type ITAM phosphorylation on 10% POPS liposomes as well as the individual tyrosine to phenylalanine CD3ζ ITAM point mutants. The third and fourth rows were used to analyze all 28ζ proteins, including the Y206F and Y209F mutants.

Figure S2: Sigmoidal fit to CD3ζ site-specific phosphorylation data.
(A) Sigmoidal fits to experimental data.
(B) Half maximal time for each CD3ζ ITAM site. Data represents mean and standard error of the mean of the fit to a 4-parameter sigmoidal curve.
(C) Hill coefficient for each CD3ζ ITAM site. Data represents mean and standard error of the mean of the fit to a 4-parameter sigmoidal curve.

Figure S3: Sequential and random order model fits
(A) Sequential order model fit to experimental data.
(B) Half maximal time for sequential order model fit.
(C) Hill coefficient for sequential order model fit.
(D) Random order model fit to experimental data.
(E) Half maximal time for random order model fit.
(F) Hill coefficient for random order model fit.

Figure S4: Additional CD3ζ ITAM site phosphorylation model fits. (A) the second biological replicate of wild type CD3ζ ITAM protein stimulated on liposomes containing 10% POPS lipids, (B) wild type CD3ζ ITAM protein stimulated on liposomes containing 0% POPS lipids, (C) wild type CD3ζ ITAM protein stimulated on liposomes containing 45% POPS lipids. (D-J) CD3ζ proteins bearing individual tyrosine to phenylalanine ITAM point mutations stimulated on liposomes containing 10% POPS lipids.

Figure S5: CD28-CD3ζ LCK binding model analysis.
(A, C, E) Heat maps showing the percent of doubly phosphorylated CD3ζ ITAMs at steady state as a function of LCK binding for each of the two tyrosine sites on ITAM A (A), ITAM B (C), and ITAM C (E). LCK binding was altered while maintaining the model fits shown in Figure 7 by changing the LCK dissociation and catalytic rates together along the contour lines shown in Figure 3. Red dashed areas indicate the parameter region in which ITAM A is significantly less phosphorylated than ITAMs B and C, representing the 21 kDa form of CD3ζ.
(B, D, F) Heat maps showing the maximum percent of bound LCK in the system over time as a function of LCK binding for each of the two tyrosine sites on ITAM A (B), ITAM B (D), and ITAM C (F).

Figure S6: Model fit of LCK initial condition. The figure on the left shows the model based on parameter from (Hui and Vale, 2014) with the LCK initial condition as calculated by LCK recombinant protein concentration estimated against an albumin standard. The figure on the right shows the initial LCK condition estimated by the model to best fit our average CD3ζ phosphorylation time course.

Table S1: List of baseline model parameters.

File S1: BioNetGen file of CD3ζ LCK phosphorylation model.

File S2: BioNetGen file of CD28 LCK phosphorylation model.

File S3: BioNetGen file of extended CD3ζ phosphorylation model with ZAP-70 binding and phosphatase activity.

Figure 1

A

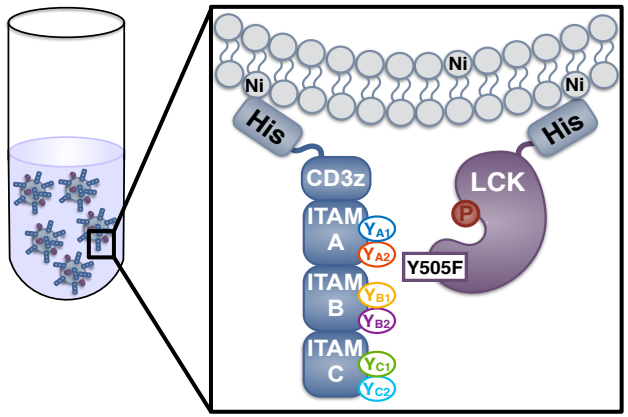

B

Y64F A1

...VK / FSR / SADAPAFQQGQNQLYNELNLGR / R /

A2

EEYDVLDK / R / R / GR / DPEMGGK / PQR / R / K /

B1 B2

NPQEGLYNELQK / DK / MAEAYSEIGMK / GER / R /

C1 C2

R / GK / GHDGLYQGLSTATK / DTYDALHMQALPPR/ ...

C

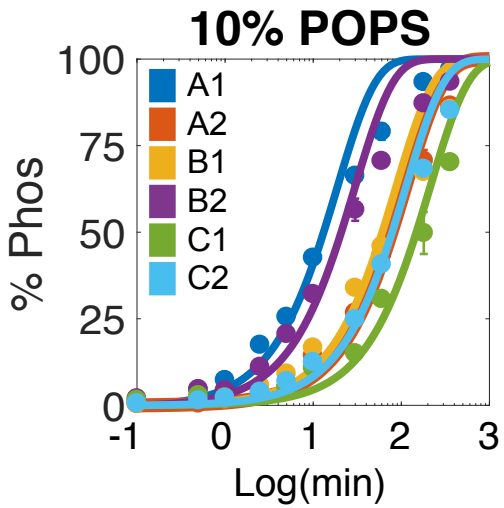

D

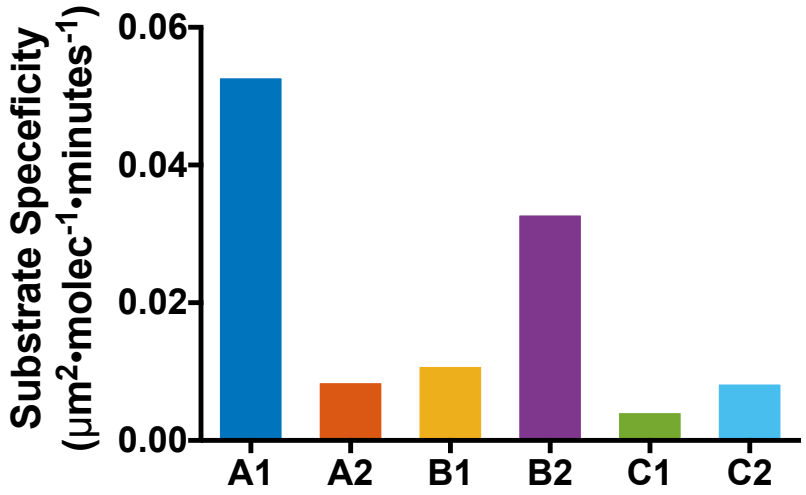

Figure 2

A

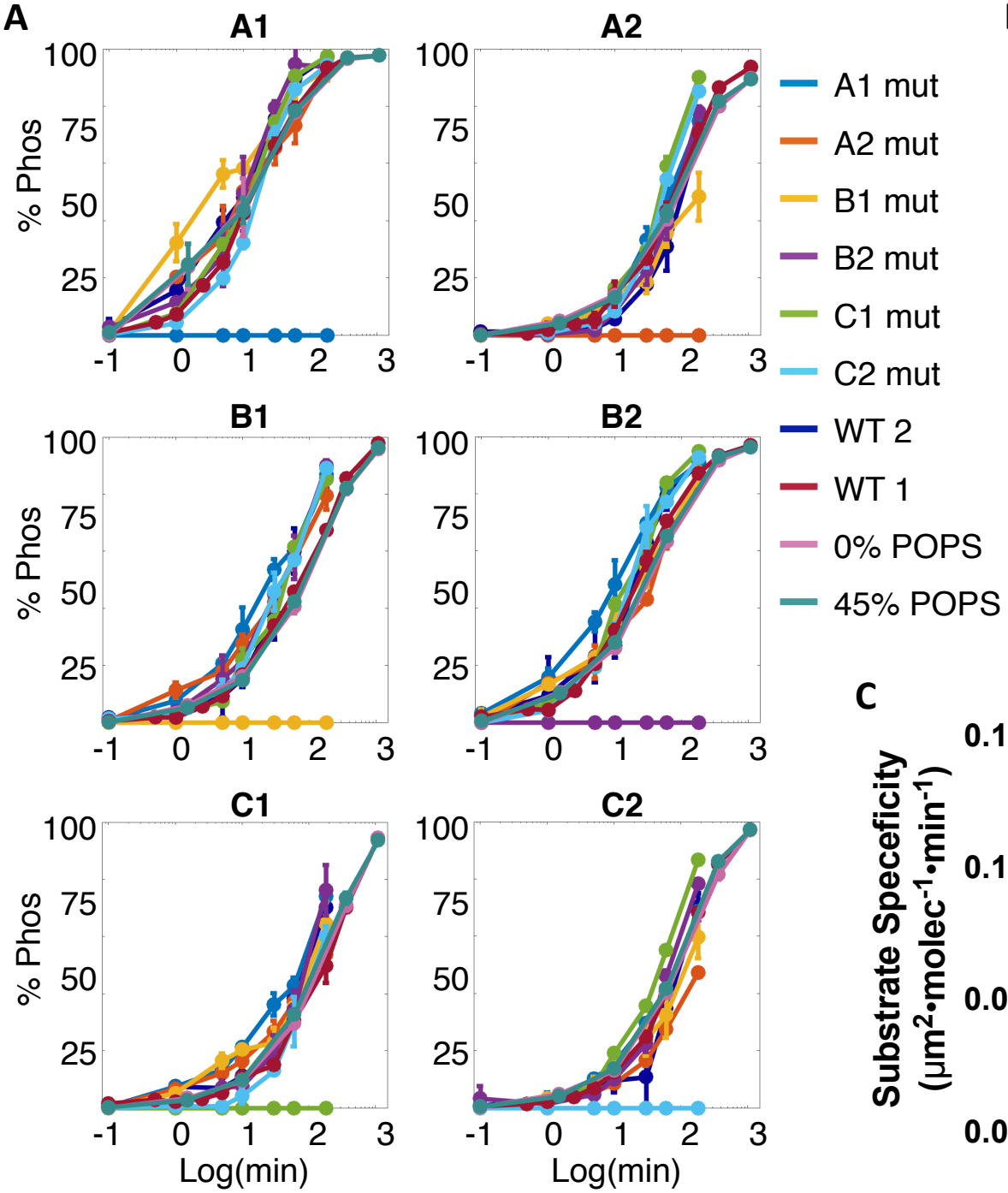

B

10 min

	A1	A2	B1	B2	C1	C2
A1		****	****	***	****	****
A2	****		*	****	n.s.	n.s
B1	****	n.s.		***	*	n.s.
B2	*	****	****		****	****
C1	****	n.s.	****	****		n.s.
C2	****	n.s.	**	****	n.s.	

60 min

C

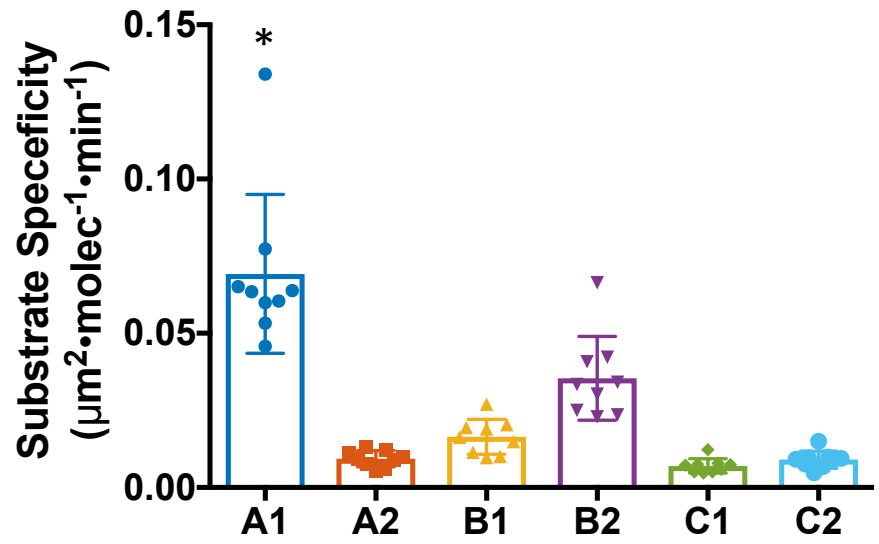

Figure 3

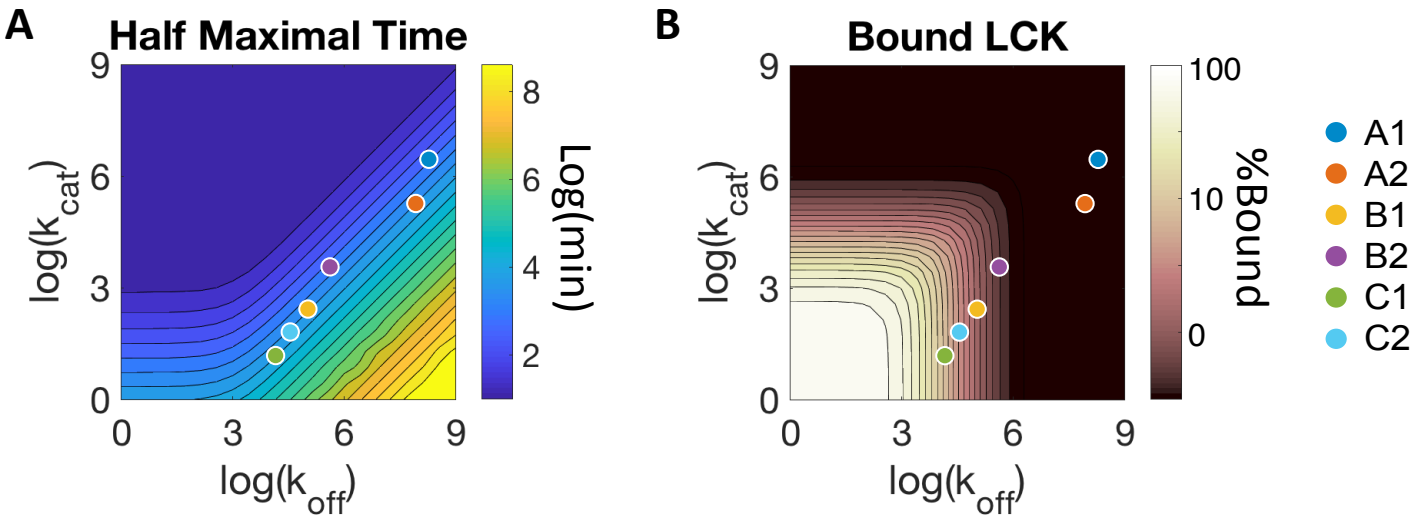
A
Half Maximal Time
log(k_cat)
log(k_off)
Log(min)
B
Bound LCK
log(k_cat)
log(k_off)
%Bound
A1
A2
B1
B2
C1
C2

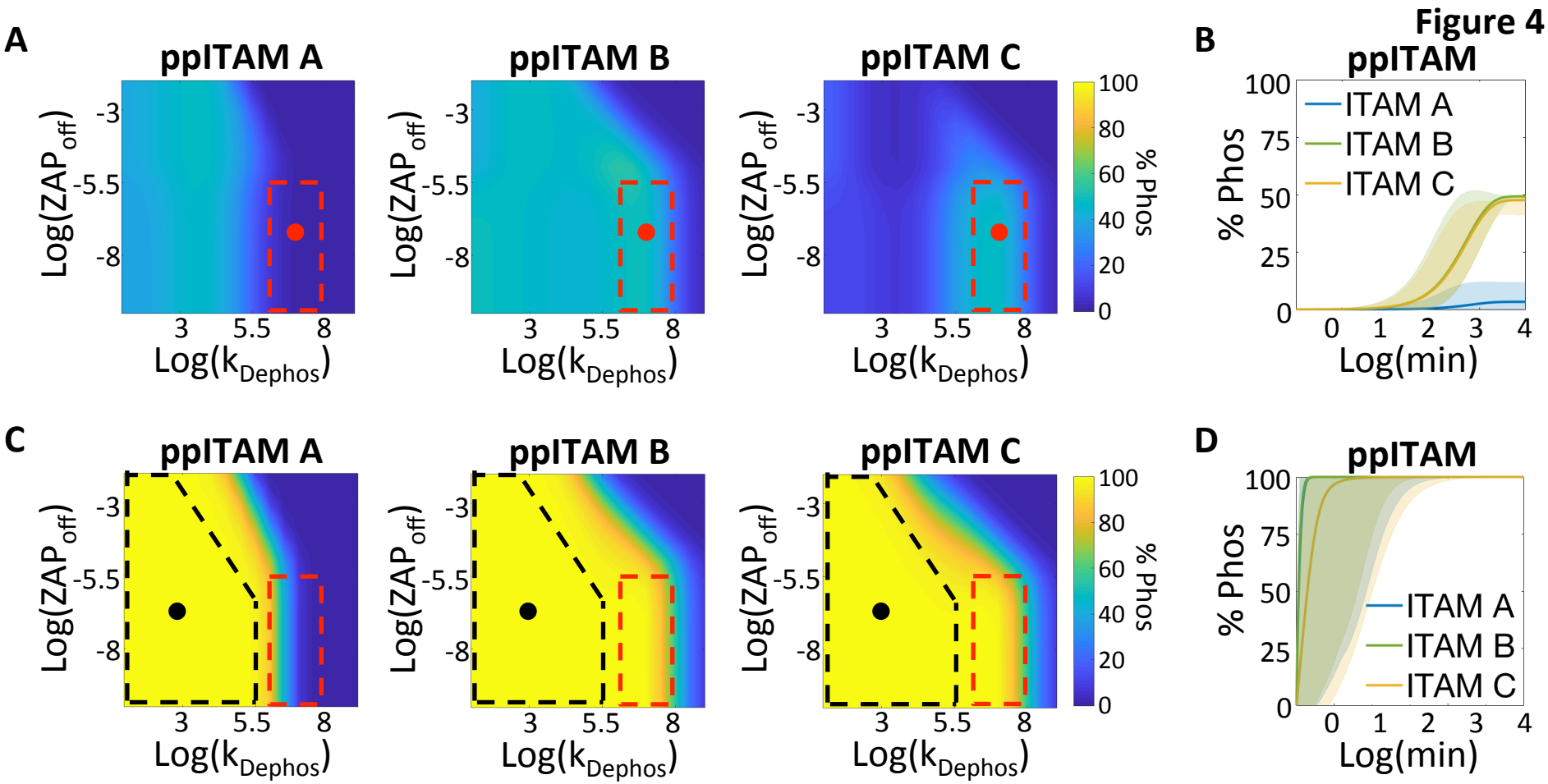
Figure 4
A
ppITAM A
ppITAM B
ppITAM C
Log(ZAP_off)
-3
-5.5
-8
3
5.5
8
Log(k_Dephos)
100
80
60
40
20
0
% Phos
B
ppITAM
ITAM A
ITAM B
ITAM C
% Phos
100
75
50
25
0
0
1
2
3
4
Log(min)
C
ppITAM A
ppITAM B
ppITAM C
D
ppITAM
ITAM A
ITAM B
ITAM C

Figure 5

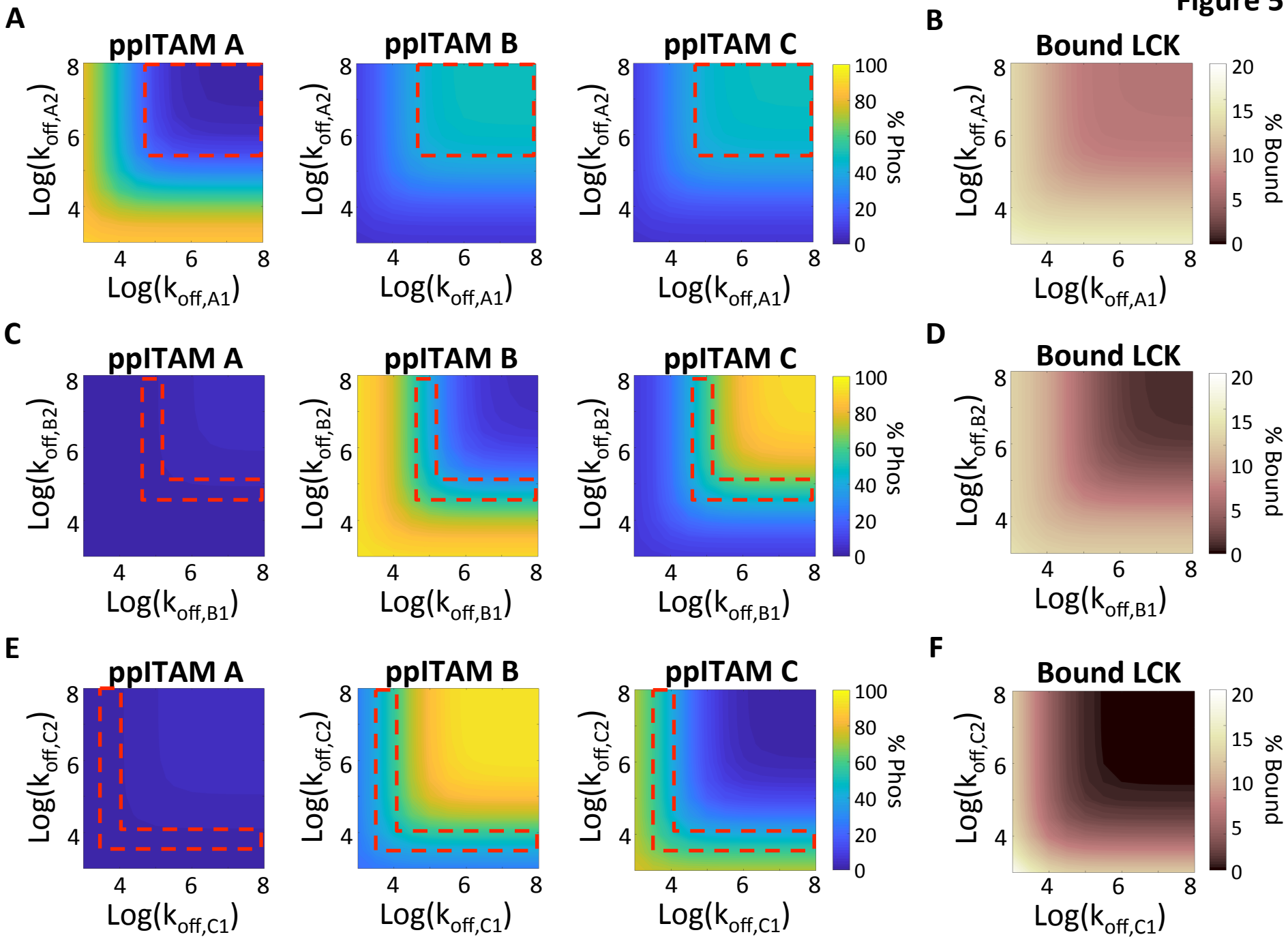
A
ppITAM A
ppITAM B
ppITAM C
B
Bound LCK
Log(k_off,A2)
Log(k_off,A1)
% phos
% Bound
C
ppITAM A
ppITAM B
ppITAM C
D
Bound LCK
Log(k_off,B2)
Log(k_off,B1)
% phos
% Bound
E
ppITAM A
ppITAM B
ppITAM C
F
Bound LCK
Log(k_off,C2)
Log(k_off,C1)
% phos
% Bound

Figure 6

A

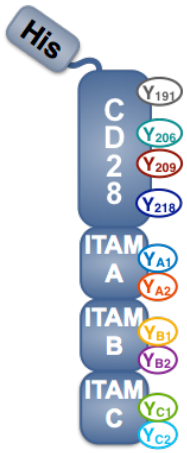

C

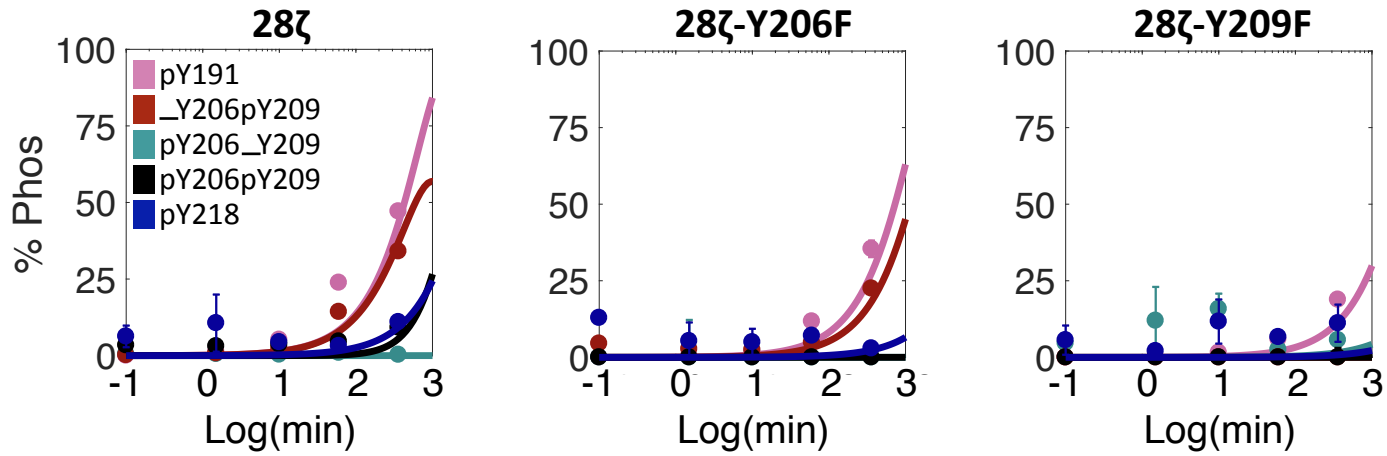

B

...R / SK / R / SR /

191

LLHSDYMNMTPR / R / PGPTR /

206 *209* *218*

KHYQPYAPPR / DFAAYR / S

D

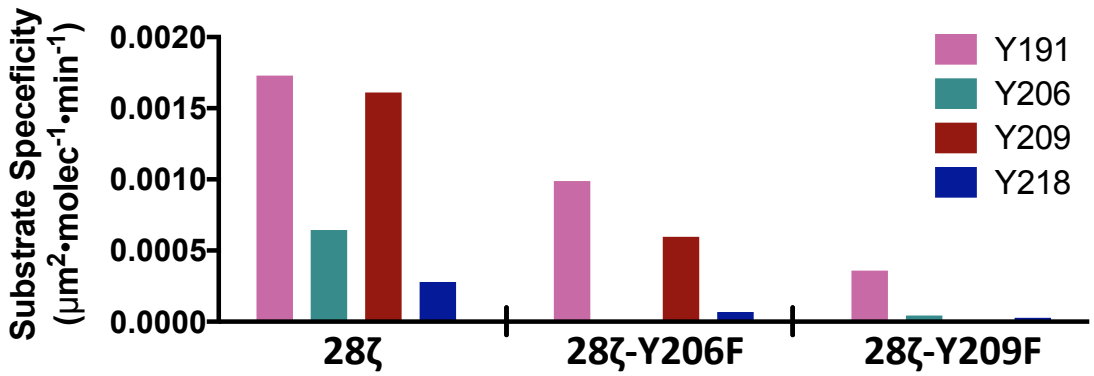

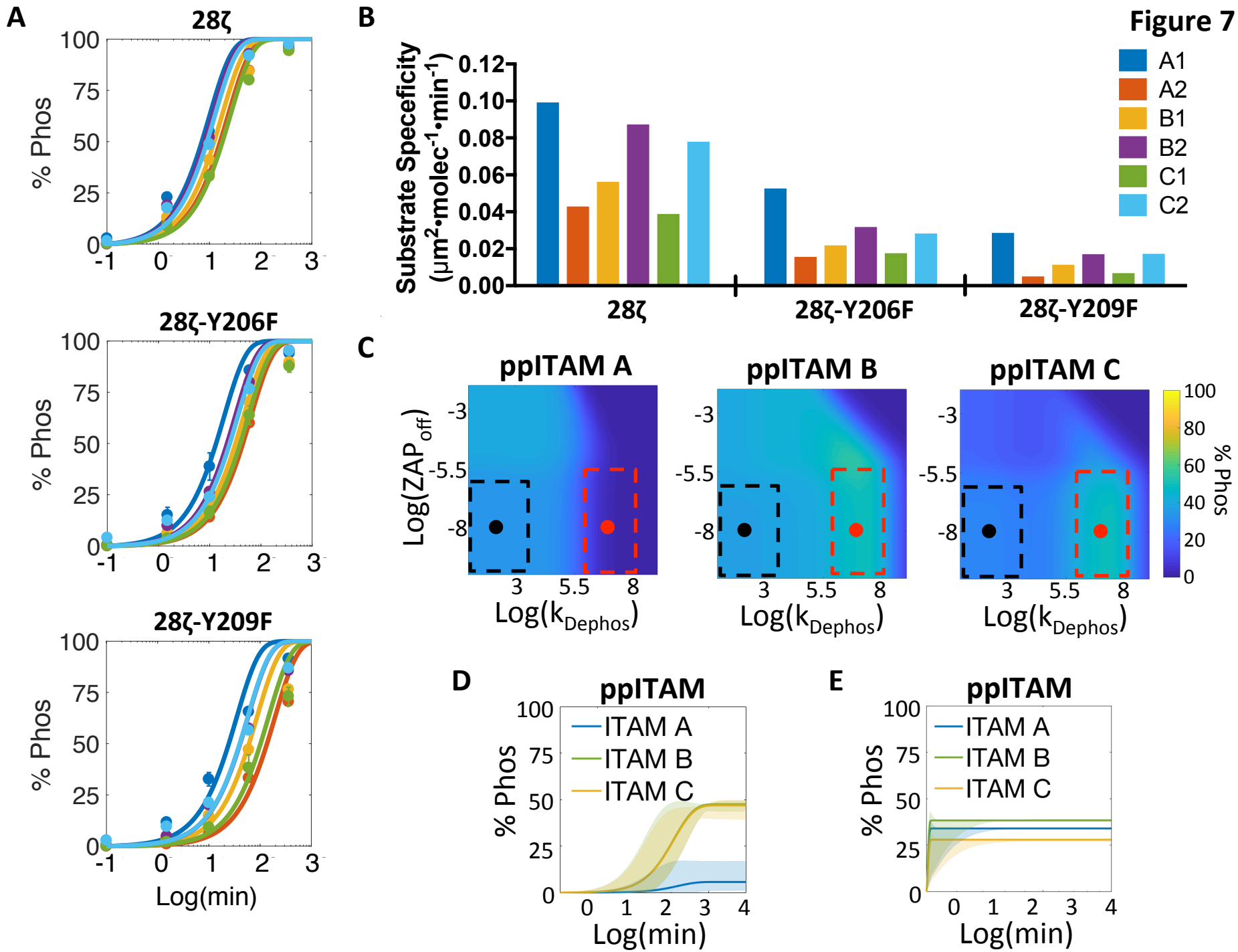
Figure 7
A
28ζ
28ζ-Y206F
28ζ-Y209F
% Phos
Log(min)
B
Substrate Speceficity
(μm²•molec⁻¹•min⁻¹)
A1
A2
B1
B2
C1
C2
C
ppITAM A
ppITAM B
ppITAM C
Log(ZAP_off)
Log(k_Dephos)
% Phos
D
ppITAM
ITAM A
ITAM B
ITAM C
E